Draft version March 20, 2014
Preprint typeset using LaTeX style emulateapj v. 5/2/11

arXiv:1403.4627v1 [astro-ph.GA] 18 Mar 2014

THE STELLAR HALOES OF MASSIVE ELLIPTICAL GALAXIES III: KINEMATICS AT LARGE RADIUS

Sudhir Raskutti [1], Jenny E. Greene[1,2], Jeremy D. Murphy[1,2]

Draft version March 20, 2014

ABSTRACT

We present a 2D kinematic analysis out to $\sim 2-5$ effective radii (R_e) of 33 massive elliptical galaxies with stellar velocity dispersions $\sigma > 150$ km s^{-1}. Our observations were taken using the Mitchell Spectrograph (formerly VIRUS-P), a spectrograph with a large 107×107 arcsec^2 field-of-view that allows us to construct robust, spatially resolved kinematic maps of V and σ for each galaxy extending to at least 2 R_e. Using these maps we study the radial dependence of the stellar angular momentum and other kinematic properties. We see the familiar division between slow and fast rotators persisting out to large radius in our sample. Centrally slow rotating galaxies, which are almost universally characterised by some form of kinematic decoupling or misalignment, remain slowly rotating in their halos. The majority of fast rotating galaxies show either increases in specific angular momentum outwards or no change beyond R_e. The generally triaxial nature of the slow rotators suggests that they formed through mergers, consistent with a "two-phase" picture of elliptical galaxy formation. However, we do not observe the sharp transitions in kinematics proposed in the literature as a signpost of moving from central dissipationally-formed components to outer accretion-dominated haloes.

1. INTRODUCTION

Much attention has been paid recently to the formation and evolution of Early-Type Galaxies [ETGs, including both elliptical (E) and lenticular (S0) galaxies], driven in large part by the discovery that ETG's at $z \sim 2$ are $\sim 2-4$ times smaller at fixed mass than their present day counterparts (van der Wel et al. 2006; di Serego Alighieri et al. 2005; Daddi et al. 2005; Trujillo et al. 2006; Longhetti et al. 2007; Toft et al. 2007; van Dokkum et al. 2008; Cimatti et al. 2008; Buitrago et al. 2008; van der Wel et al. 2008; Franx et al. 2008; van Dokkum et al. 2008; Damjanov et al. 2009; Cenarro & Trujillo 2009; Bezanson et al. 2009; van Dokkum et al. 2010; van de Sande et al. 2011; Whitaker et al. 2012). To explain the rapid size evolution from $z \sim 2$ until today, a two-phase picture of ETG growth has emerged. At early times, ETG's form in a highly dissipative environment, with rapid star formation creating massive, compact cores, where most of the stars formed in situ (Kereš et al. 2005; Khochfar & Silk 2006; De Lucia et al. 2006; Krick et al. 2006; Naab et al. 2007; Naab et al. 2009; Joung et al. 2009; Dekel et al. 2009; Kereš et al. 2009; Oser et al. 2010; Feldmann et al. 2010; Domínguez Sánchez et al. 2011; Feldmann et al. 2011; Oser et al. 2012). The second phase, dry accretion, is dominated by collisionless dynamics during which star formation is suppressed and most of the stellar mass increase occurs in the galactic outskirts (Hopkins et al. 2009; van Dokkum et al. 2010; Szomoru et al. 2012; Saracco et al. 2012).

While such a two-phase picture is generally compelling, it is uncertain precisely how and when mass is added (e.g., the balance of major to minor mergers). Simple virial arguments (Cole et al. 2000; Naab et al. 2009; Bezanson et al. 2009) as well as recent cosmological simulations (Hilz et al. 2012; Oogi & Habe 2013; Hilz et al. 2013) suggest that major and minor mergers have very different effects. Violent relaxation in major mergers generally results in moderate, factor of $\sim 2-3$, increases in the half-mass radius for every merger event. Meanwhile, mass build-up via minor mergers deposits more mass in the outskirts, resulting in $\sim 5-$fold increases in the radius for similar growth in mass (Hilz et al. 2012). Simulations therefore currently favor a 1 : 5 mass ratio in mergers (Oser et al. 2012; Lackner et al. 2012; Gabor & Davé 2012). However, incomplete modelling of feedback processes (e.g., AGN and supernovae winds) makes these results uncertain.

Kinematic observations of local ellipticals also contain important information. It has long been known that ETG's are well separated into those that rotate and those that do not (e.g., Bertola & Capaccioli 1975; Illingworth 1977; Davies et al. 1983). The former tend to have lower stellar mass, disky isophotes and cuspy light profiles, while the latter are triaxial, cored, and massive (e.g., Bender et al. 1989; Kormendy & Bender 1996; de Zeeuw 1985; Franx et al. 1991; de Zeeuw & Franx 1991; van den Bosch et al. 2008). Modern integral-field studies have provided strong confirmation of this general bimodal picture with excellent statistics (e.g., Emsellem et al. 2004; Cappellari et al. 2007; Emsellem et al. 2007; Krajnovic et al. 2011; Cappellari et al. 2011; Emsellem et al. 2011) and have made interesting comparisons with cosmological simulations (Khochfar et al. 2011; Davis et al. 2011; Serra et al. 2014).

In the context of two-phase assembly, it is thought that the global properties of each family can be linked to their formation history. Slow Rotators (SRs) are thought to accrete most of their mass in minor dry mergers with up to ~ 3 major mergers (Khochfar et al. 2011). This explains both their low net rotation and their preponderance of kinematically decoupled cores that are likely long-lived remnants of mergers (KDC, e.g., Kormendy 1984; Forbes et al. 1994; Carollo et al. 1997; Emsellem et al. 2004; Emsellem et al. 2007; Krajnović et al. 2008). In contrast Fast Rotators (FRs) likely grew predomi-

[1] Department of Astrophysics, Princeton University,
[2] Department of Astronomy, UT Austin, 1 University Station C1400, Austin, TX 71712

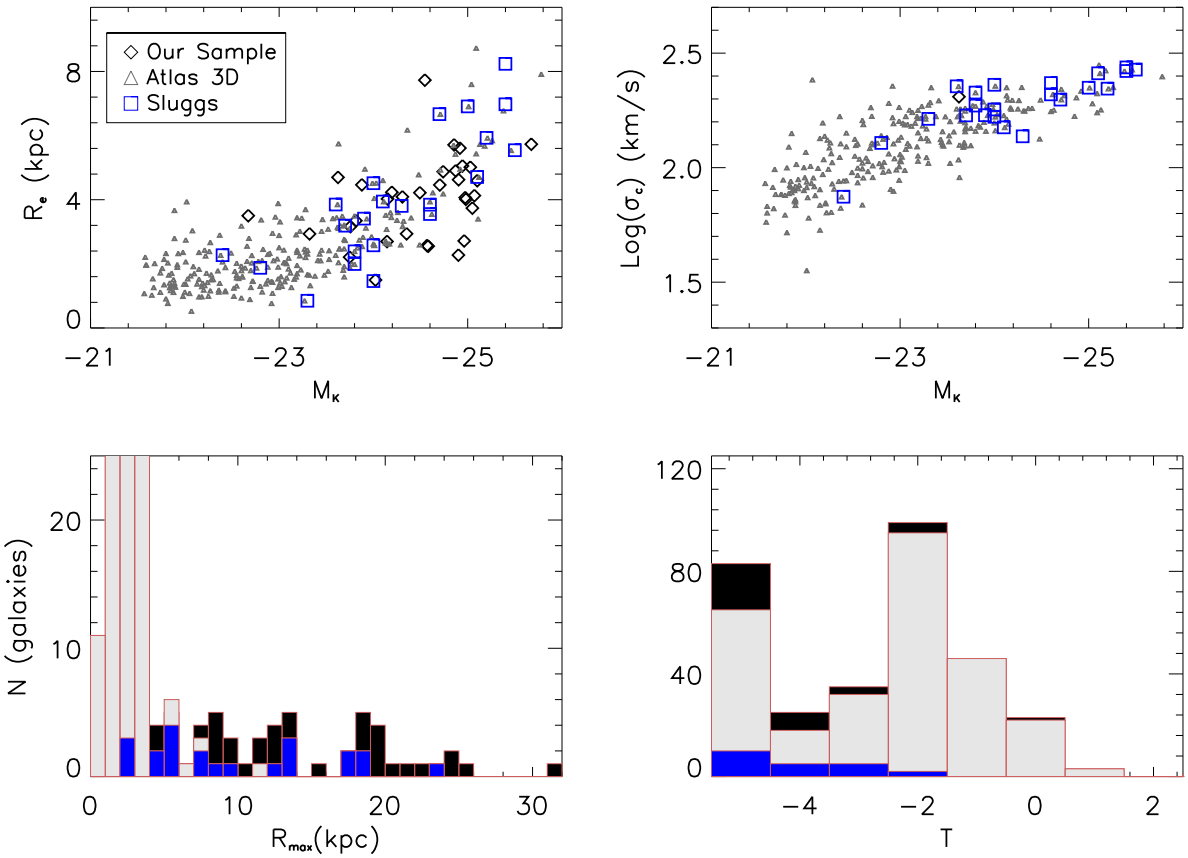

Figure 1. Characteristics of our galaxy sample (black) as compared to the volume-limited ATLAS^{3D} survey of ETG's (grey Cappellari et al. 2011) and the 22 massive galaxies in the SLUGGS survey (blue Arnold et al. 2013). We show the K-band magnitude and half-light radii (top left panel), the distribution of central dispersions (σ_c) as a function of luminosity (top right panel), the distribution of maximum observed radii (bottom left) and the distribution of Hubble Types (bottom right). We note that the radii are measured by the SDSS for our galaxies using a deVaucouleurs fit to the light profile, while they are based on RC3 for the ATLAS^{3D} and SLUGGS galaxies. For clarity, we have truncated the histogram at bottom left. In the truncated bins, there are 120, 95 and 30 ATLAS^{3D} galaxies respectively.

nantly through cold gas accretion with at most one major merger (Bois et al. 2011; Khochfar et al. 2011; Davis et al. 2011; Serra et al. 2012), and thus have high rotation velocities.

However, this picture remains uncertain since most observations are limited to within the half-light radius of the galaxy. In contrast, if late-stage growth occurs through dry accretion, then most of the dynamical changes occur beyond the half-light radius, where stars have longer relaxation times and so carry a record of the merger history (van Dokkum 2005; Duc et al. 2011; Romanowsky & Fall 2012). It is also only in the outer regions that observations become sensitive to dark matter, for which there are concrete predictions from cosmological simulations. Therefore, wide-field kinematic data are required to provide more direct signatures of two-phase growth.

A number of kinematic measurements of ETG's out to large radius have been made using spatially sparse measurements of planetary nebulae (PNe) and globular clusters (GCs) (Méndez et al. 2001; Coccato et al. 2009; Strader et al. 2011; McNeil-Moylan et al. 2012; Arnold et al. 2011; Pota et al. 2013). Most recently, Arnold et al. (2013) presented spatially well-sampled measurements of 22 massive ETG's out to $\sim 4R_e$ as part of the SLUGGS survey. They showed that a significant fraction of their galaxies (particularly Es) show a transition from rotation to dispersion-dominated beyond $\sim R_e$. They interpreted this as a transition between a central dissipational component, formed at early times, and an outer halo-dominated region formed through later dry merging.

However, without full 2D kinematic coverage from integral-field spectroscopic (IFS) studies of stellar continua, these results alone can be difficult to interpret. Thus far, at large radius, most studies of stellar kinematics either utilize one or two long-slit positions (Carollo & Danziger 1994; Thomas et al. 2011), or focus on individual objects with IFS (e.g., Weijmans et al. 2009; Proctor et al. 2009; Coccato et al. 2010; Murphy et al. 2011). By contrast, Greene et al. (2012); Greene et al. (2013) assembled a sample of 33 massive, local ETG's with observations extending over $\sim 2-4R_e$. They studied stellar population gradients, finding that most stars in the outskirts were comparatively old and metal-poor, consistent with accretion from much smaller galaxies. While they were able to constrain when the stars at large radius formed, dynamical studies are much better suited to revealing where they were formed and how they were assembled.

In this study, we therefore extend the Greene et al. survey by studying the stellar kinematics in conjunction with the stellar populations. We begin in §2 by briefly discussing the galaxy sample, before describing in §3 our observations, reduction methods and dynamical modelling. In §4 we discuss the basic kinematic characteristics of our galaxies at large radius, with particular reference to the Slow and Fast Rotator paradigm. We then go on to explore, in §5, the possible theoretical implications of our results before concluding in§6.

2. THE GALAXY SAMPLE, OBSERVATIONS, AND DATA REDUCTION

The observations analyzed here were taken with the George and Cynthia Mitchell Spectrograph (the Mitchell Spectrograph, formerly VIRUS-P; Hill et al. 2008) on the 2.7m Harlan J. Smith telescope at McDonald Observatory. The Mitchell Spectrograph is an integral-field spectrograph composed of 246 fibers covering a $107'' \times 107''$ field of view with a one-third filling factor. Each of the 246 fibers subtends $4\farcs2$ and they are assembled in an array similar to Densepak (Barden et al. 1998). The Mitchell Spectrograph has performed a very successful search for Lyα emitters (Adams et al. 2011; Finkelstein et al. 2011; Blanc et al. 2011) and has become a highly productive tool to study spatially resolved kinematics and stellar populations in nearby galaxies (Blanc et al. 2009; Yoachim et al. 2010; Murphy et al. 2011; Adams et al. 2012).

We use the low-resolution (R $\approx$ 850) blue setting of the Mitchell Spectrograph. Our wavelength range spans 3550-5850 Å with an average spectral resolution of 5 Å FWHM. This resolution delivers a dispersion of $\sim$ 1.1 Å pixel^{-1} and corresponds to $\sigma \approx 150$ km s^{-1} at 4300 Å, our bluest Lick index. Each galaxy was observed for a total of $\sim$ 2 hours on source with one-third of the time spent at each of three dither positions to fill the field of view. Initial data reduction is accomplished using the custom code Vaccine (Adams et al. 2011; Murphy et al. 2011), which performs basic bias subtraction, wavelength calibration, cosmic-ray rejection, sky subtraction, and spectral extraction. Final processing and flux calibration is performed using code developed for the VENGA project (Blanc et al. 2009, 2013). The details of our data reduction are described in Murphy et al. (2011), Greene et al. (2012) and Murphy et al. (2013).

Properties of the entire sample of massive galaxies are shown in Table 1. The sample, selected from the SDSS (York et al. 2000), is identical to that presented in Greene et al. (2013), and details of the selection criteria can be found there. However, briefly, galaxies were chosen to have central stellar velocity dispersions $\sigma_c > 150$ kms^{-1}, to be observable in a single $107'' \times 107''$ pointing, and to have $u - r > 2.2$ (Strateva et al. 2001). We then removed spiral galaxies by hand. Finally, only galaxies with half-light radii at least twice the fiber diameter of $4\farcs2$ were included.

Figure 1 shows some of the key characteristics of our sample compared to that of the volume-limited ATLAS^{3D} survey as well as the more recent SLUGGS survey. By focusing on high stellar velocity dispersion, we have deliberately selected a population of more massive and more distant ellipticals than the ATLAS^{3D} and SLUGGS samples. As a result of their distance they also tend to be more compact on the sky.

We also show the distribution of maximum radii $R_{\rm max}$, defined as the exterior radius of the outermost spatial bins (Figure 1). Beyond $R_{\rm max}$ we cannot achieve our limiting signal-to-noise ratio (S/N) of 15 even in bins extending over half the face of the galaxy and with a width of R_e. Our maximum radii extend well beyond the ATLAS^{3D} sample in both kpc and R_e, and achieve comparable depth to the SLUGGS sample. However, we mention two caveats. First, as in our prior papers we adopt the SDSS "model" radius (based mostly on the de Vaucouleurs fit; de Vaucouleurs 1948; Graham et al. 2005) as the effective radius (R_e). In principle, galaxy profile shape is a function of mass (e.g., Caon et al. 1993; Kormendy et al. 2009), but fitting the galaxies with a fixed Sersic (n) index of four has the benefit that we are less sensitive to both sky subtraction errors (Mandelbaum et al. 2005; Bernardi et al. 2007) and to the detailed shape of the light profile in the very faint wings (e.g., Lackner & Gunn 2012). In the effort to have a uniform analysis, we have therefore adopted the effective radii published by the SDSS, which tend to be small compared to literature values. Furthermore, our outermost radii correspond to measurements over wide bins in both the radial (R_e) and azimuthal (π) directions, and so it is worth bearing in mind that while we reach large radius we do so at low spatial resolution.

Finally, we will often examine properties of our sample as a function of stellar mass. Stellar masses are based on the stellar population synthesis presented in Greene et al. (2013) based on Lick index modeling within $\sim R_e$ (Graves & Schiavon 2008). Using the α-enhanced models of Schiavon (2007), SDSS r-band photometry, and assuming a Salpeter IMF, we derive a luminosity-weighted global M/L. The inferred stellar masses are subject to systematics from emission-line contamination, which primarily impacts Hβ and therefore the stellar ages (e.g., Graves et al. 2007). As a sanity check, we extract K-band luminosities from the 2MASS Extended Source Catalog (XSC, available online[3] Huchra et al. 2012), and use the empirical scaling of Cappellari (2013) based on kinematics to calculate an independent stellar mass. We find agreement within $\sim$ 30% in all cases. Given the order of magnitude range probed by our galactic sample, we are therefore able to robustly separate galaxies into mass bins.

3. ANALYSIS: KINEMATIC MODELLING

We briefly outline here the higher-level analysis (source masking and binning) involved in preparing the data for kinematic measurements. We then describe the extraction of kinematic parameters using the penalised PiXel Fitting (pPXF) technique of Cappellari & Emsellem (2004).

3.1. *Source Masking*

Before coadding or fitting any spectra, we first mask out any fibers on the IFU that are dominated by foreground sources. Close to half of our galaxies (NGC 219, NGC 661, NGC 677, IC 301, NGC 1286, IC 312, NGC 1267, NGC 3837, NGC 3842, NGC 4065, NGC 4952, NGC 6127, NGC 6964, NGC 7509,

[3] http://www.ipac.caltech.edu/2mass.

Table 1
Galaxy Sample

Galaxy	RA	Dec	z	Mag	Morph.	PA	ϵ	R_e	σ_c	Env
(1)	(2)	(3)	(4)	(5)	(6)	(7)	(8)	(9)	(10)	(11)
NGC 219	00:42:11.3	+00:54:16.3	0.018	15.0	−5.0	172.0	0.11	4.4	184	F
NGC 426	01:12:48.6	-00:17:24.6	0.018	14.0	−2.5	150.0	0.32	8.3	285	F
NGC 474	01:20:06.6	+03:24:55.8	0.008	12.4	−2.17	4.9	0.19	18.1	163	F
CGCG 390-096	03:30:17.1	−00:55:12.6	0.021	14.7	−5.0	61.8	0.13	7.8	204	F
NGC 661	01:44:14.6	+28:42:21.1	0.013	13.2	−4.0	50.1	0.36	19.9	190	G
NGC 677	01:49:14.0	+13:03:19.1	0.017	13.7	−5.0	0.6	0.13	9.6	257	G
UGC 1382	01:54:41.0	−00:08:36.0	0.019	14.3	−5.0	65.0	0.25	9.9	195	F
NGC 774	01:59:34.7	+14:00:29.5	0.015	13.8	−2.2	165.4	0.24	20.9	165	F
IC 301	03:14:47.7	+42:13:21.6	0.016	14.2	−4.7	148.0	0.21	12.6	159	C
NGC 1286	03:17:48.5	−07:37:00.6	0.014	14.1	−4.0	151.5	0.19	18.1	163	F
IC 312	03:18:08.4	+41:45:15.6	0.017	14.4	−4.0	124.9	0.49	18.1	218	C
NGC 1267	03:18:44.7	+41:28:02.8	0.018	15.4	−3.3	51.7	0.15	6.4	236	C
NGC 1270	03:18:58.1	+41:28:12.4	0.017	14.3	−5.0	179.1	0.20	6.4	373	C
NVSS	03:20:50.7	+41:36:01.5	0.018	15.5	−5.0	131.7	0.18	4.5	274	C
UGC 4051	07:51:17.6	+50:10:45.4	0.021	14.2	−5.0	13.1	0.19	8.6	300	G
NGC 3837	11:43:56.4	+19:53:40.4	0.021	14.4	−5.0	109.9	0.26	8.1	265	C
NGC 3482	11:44:02.1	+19:56:59.3	0.021	13.5	−5.0	176.9	0.19	20.5	284	C
NGC 4065	12:04:06.1	+20:14:06.2	0.021	13.6	−5.0	108.4	0.17	12.5	278	C
IC 834	12:56:18.5	+26:21:32.0	0.021	14.6	−4.3	97.7	0.35	7.3	255	F
NGC 4908	13:00:54.4	+28:00:27.4	0.017	14.1	−4.0	102.2	0.31	18.5	236	F
NGC 4952	13:04:58.3	+29:07:20.0	0.020	13.6	−4.1	21.5	0.36	12.1	292	F
NGC 5080	13:19:19.2	+08:25:44.9	0.022	14.6	−2.0	93.4	0.09	7.8	269	F
NGC 5127	13:23:45.0	+31:33:57.0	0.016	13.3	−4.8	71.2	0.27	22.9	275	F
NGC 5423	14:02:48.6	+09:20:29.0	0.020	13.7	−3.3	75.9	0.33	10.9	263	G
NGC 5982	15:38:39.8	+59:21:21.0	0.010	12.1	−5.0	102.5	0.30	17.9	239	F
IC 1152	15:56:43.3	+48:05:42.0	0.020	13.9	−5.0	28.0	0.17	7.7	258	G
IC 1153	15:57:03.0	+48:10:06.1	0.020	13.6	−2.8	165.4	0.19	9.8	241	G
CGCG 137-019	16:02:30.4	+21:07:14.5	0.015	14.2	−4.0	18.3	0.15	8.7	174	F
NGC 6127	16:19:11.5	+57:59:02.8	0.016	13.0	−5.0	33.8	0.03	11.2	247	F
NGC 6482	17:51:48.8	+23:04:19.0	0.013	12.4	−5.0	65.0	0.15	9.7	292	G
NGC 6964	20:47:24.3	+00:18:02.9	0.013	13.8	−4.9	23.2	0.13	17.0	188	G
NGC 7509	23:12:21.4	+14:36:33.8	0.016	14.1	−5.0	175.8	0.07	9.0	180	F
NGC 7684	23:30:32.0	+00:04:51.8	0.017	13.7	0.25	153.5	0.47	15.8	169	F

Notes: Col. (1): Galaxy Name. Col. (2): RA (hrs) in J2000. Col. (3): Dec (deg) in J2000. Col. (4): Redshift from the SDSS. Col. (5) $g-$band magnitude (mag) from the SDSS. Col. (6): morphological T type from HyperLeda. E: $T \leq -3.5$; S0: $-3.5 < T \leq -0.5$. Col. (7): SDSS photometric position angle (deg). Col. (8): SDSS photometric ellipticity. Col. (9): SDSS major axis half-light radius (″). Col. (10): SDSS stellar velocity dispersion (kms^{-1}). Col. (11): We sort galaxies into Field, Group, and Cluster based on the number of group members in the Yang et al. (2007) catalogue as described in Greene et al. (2013). Field galaxies have $N_{\mathrm{group}} < 5$, group indicates $5 < N_{\mathrm{group}} < 50$, and cluster indicates richer than 50 group members.

NGC 7684) require masking of some sort beyond R_e, though in most cases the external sources are not extended and so do not affect more than one or two fibers.

Two galaxies, NGC 1267 and NGC 6482, also have bright stars between us and the galaxy center, which contaminate 4 or 5 fibers in the core. Kinematic measurements are therefore not able to probe to radii within $\sim 0.5R_e$ for these galaxies. Finally, we note that a small number of galaxies, most notably NGC 426 and NGC 7509, have central fibers dominated by strong emission lines characteristic of AGN, which can affect measurements of dispersion. However, we choose not to mask out these fibers, but instead deal with the emission lines in our fitting procedure (see Appendix).

3.2. *Spatial Binning*

We require a minimum S/N of 15 (justified in the Appendix) to extract robust kinematics, but only the very central individual fibers have such high S/N. Therefore, we must perform our analysis on radially binned spectra. All spectra are resampled onto a common wavelength grid over the range 4000 Å$< \lambda <$ 5420 Å. Both spectra and errors are then weighted by their flux, coadded, and renormalised. We use flux-weighted addition with iterative sigma-clipping, which provides a simple and reliable estimate of the coadded errors. The spectra combined in this manner are nearly identical to those derived from the biweight estimator (Beers et al. 1990) employed in Murphy et al. (2011).

The size of each spatial bin is set by the minimum S/N requirement. The innermost fibers that pass this threshold are analysed without further coaddition. We then bin in elliptical annuli set by the axial ratio measured from SDSS. Each radial bin begins with a width of 0.5 R_e along the major axis and is further separated into 5 angular bins in each quadrant, each with equal width in $\sin\theta$. Spectra are folded across the minor axis, so that we are left with 10 angular bins in total (Gebhardt et al. 2000, 2003; McConnell et al. 2012). When an angular bin falls below the S/N threshold, it is merged with its nearest neighbors until we are left with only two angular bins, one on each side of the major axis, at a given radius. If more binning is required, then the size of the bin is increased radially by 0.1 R_e until we cross the S/N threshold or the edge of the integral-field unit (IFU) is reached. With this procedure we are typically able to probe out to ~ 4 R_e with full angular information available only for the inner bins.

Figure 2 demonstrates our binning scheme. In the case of the spatially extended galaxy NGC 4952, shown in the top panel of Figure 2, we are able to retain many individual fibers and then eventually end with five purely radial bins of varying width. Even here, we can only resolve angular structure out to ~ 1.5 R_e, while the outermost bin runs over the edge of the IFU. NGC 426 (bottom), while still quite massive, is one of our smallest galaxies on the

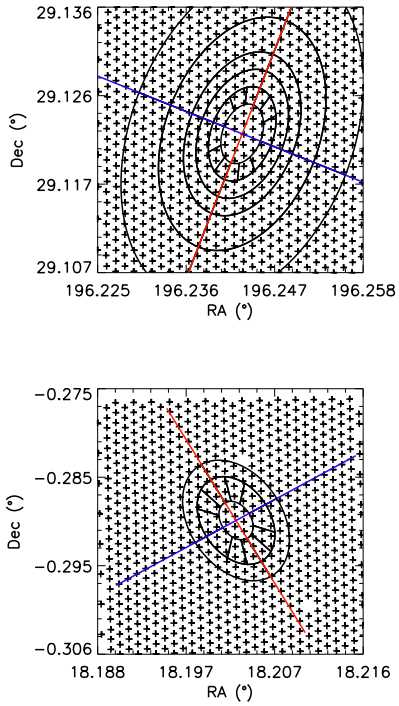

Figure 2. Locations of bins for galaxies NGC 4952 (top) and NGC 426 (bottom). We show fiber positions for one dither (crosses), bin locations, and the major (red) and minor(blue) axes. Radial bins vary in size between 0.5 and 1 R_e. We note that a typical observation involves 3 dithers of the IFU so that sky coverage is 3 times denser than shown.

sky. It has a much smaller inner region, and only 3 radial bins. Nevertheless, because the galaxy is so compact, we are able to probe out to $\sim 3\ R_e$.

3.3. *Kinematics*

In principle, stellar velocity dispersions can be measured in a number of ways, including Fourier techniques such as the cross-correlation (Tonry & Davis 1979) and the Fourier quotient (Simkin 1974; Sargent et al. 1977). However, now that computational costs are no limitation, direct pixel-by-pixel fitting (Burbidge et al. 1961; Rix & White 1992) allows for masking of emission lines and does not suffer from windowing problems. We employ the direct fitting pPXF technique of Cappellari & Emsellem (2004) to calculate our stellar kinematics. In brief, pPXF convolves a library of stellar templates with a line-of-sight velocity distribution (LOSVD) function that is modeled as a Gauss-Hermite series (van der Marel & Franx 1993; Gerhard 1993):

$$\mathcal{L}(v) = \frac{e^{-(1/2)y^2}}{\sigma\sqrt{2\pi}}\left[1 + \sum_{m=3}^{M} h_m H_m(y)\right] \qquad (1)$$

where $y = (v - V)/\sigma$ and the H_m are the Hermite polynomials. The free LOSVD parameters $\{V, \sigma, h_i\}$ are fit by minimizing over a given objective function using the Levenberg-Marquardt method for non-linear least squares problems. The objective function itself is regularised to favour gaussian profiles so that

$$\chi^2_{\rm p} = \chi^2\,(1 + \lambda^2\mathcal{D}^2),$$
$$\mathcal{D}^2 \approx \sum_{m=3}^{M} h_m^2. \qquad (2)$$

with $\lambda \sim 0.7$ found to work well empirically (Cappellari et al. 2011). We find no significant deviations from Gaussian LOSVDs in our data, so we simply set $\lambda = 0$, or equivalently fix all hermite moments to zero, and the problem reduces to pixel-fitting by standard χ^2 minimisation with a Gaussian LOSVD. We fit over a large wavelength range that starts just redward of the 4000 Å break and extends to the Fe lines at 5420 Å. Over this region the continuum is well-modelled with multiplicative Legendre polynomials of order 10, and the presence of emission lines has little systematic effect on the derived kinematics. A more detailed justification for our choice of wavelength region, continuum polynomial degree, and LOSVD can be found in the Appendix.

Errors for our Gaussian fits were estimated using a Monte-Carlo method. We started with the noiseless fit to each spectrum and added Gaussian-distributed noise to each pixel according to its error array. The new noisy spectrum was then fit using pPXF. When repeated over many realizations of the added noise, this produces an estimate of the errors in our fits to V and σ. In a small number of galaxies, measured dispersions fell well below the instrumental dispersion ($\sigma \lesssim 100$ km s^{-1}), and measured errors approached $\sim 20\%$. These measurements were deemed unreliable and ignored in all further analysis.

Our stellar templates were chosen from stellar population synthesis (SPS) spectra, as generated by the Flexible SPS (FSPS) code (Conroy et al. 2009) calibrated to the observational data in Conroy & Gunn (2010), with an intrinsic resolution of 2.5 Å FWHM. Since pPXF is sensitive to the completeness of the stellar library (Cappellari et al. 2011) we adopted a wide range of ages, 3 Gyr $< t <$ 13.5 Gyr and alpha-enhancements, $0.0 < [\alpha/Fe] < 0.4$, alongside a Chabrier IMF for our template library. We then allowed each binned spectrum to fit to a weighted sum of these templates. We used SPS models rather than stars to gain some additional insight into the stellar populations of our galaxies. However, we did cross-compare with stellar templates, and examine our sensitivity to template mismatch in detail, with resulting systematic errors in our kinematic estimates of $\sim 10 - 20$ kms^{-1}.

3.4. *Robustness of the Kinematic Fits*

Our extracted kinematics are subject to both statistical errors and systematic uncertainties in the continuum, the degree of non-gaussianity in our LOSVD, the choice of stellar templates, and the presence of emission lines in certain galaxies. We therefore tested the robustness of our kinematic fits to all of these uncertainties in Appendix A. As a summary, we show in Figure 3 example fits to the central and outermost fibers in NGC 4952 and NGC 426. We see that the effects of template mismatch are relatively small, though not entirely negligible, especially in the case of NGC 426.

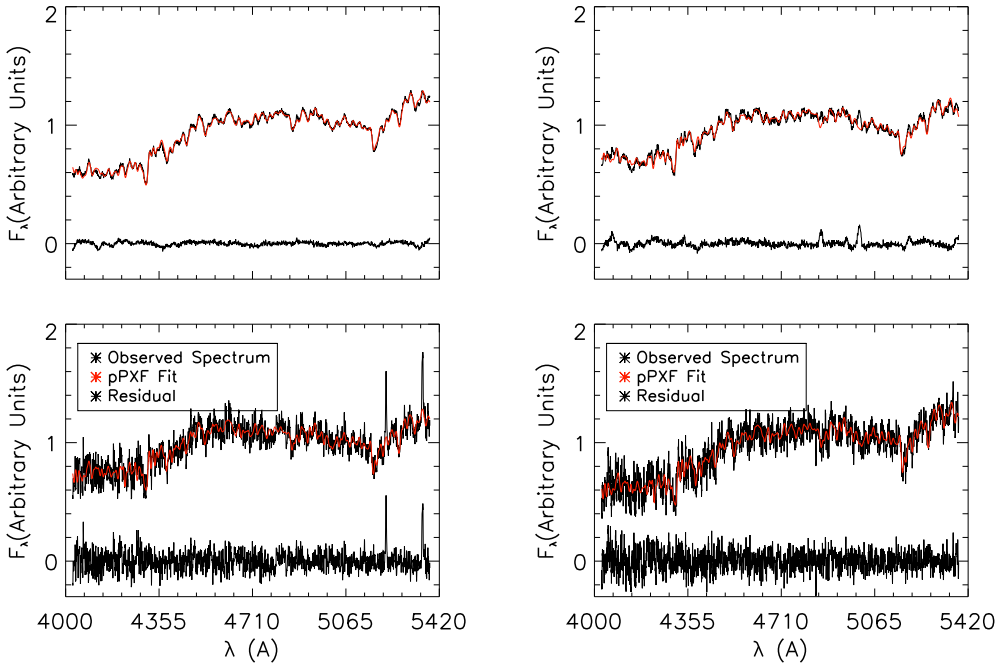

Figure 3. Spectra and pPXF fits for the central (top) and outermost (bottom) bins in NGC 4952 (left) and NGC 426 (right) over our fiducial wavelength range. The fit for NGC 4952 especially suffers no issues with template mismatch even at low S/N.

We also show comparisons of our central velocity dispersions to literature data in Figure 4. Almost all of our galaxies have dispersions in the SDSS catalog (Blanton et al. 2005), and we supplement these with the lists compiled by Whitmore et al. (1985), McElroy (1998) and most recently Ho et al. (2009). We match the SDSS aperture relatively well, while the Ho et al. (2009) measurements had a similar 2″ by 2 ″ aperture, and the Whitmore et al. (1985) and McElroy (1998) compilations were placed on a 2″ by 4″ system. As can be seen from Figure 4, we find a small systematic negative bias in our dispersion calculations of around 20 km s^{-1} on average. The low resolution of our fibers means that we blend dispersions out to larger radius than SDSS and so expect to find systematically smaller dispersions. Furthermore, this bias is typically less than $\sim 2\sigma$ and is much smaller than the large measured dispersions of $\gtrsim 150$ km s^{-1}.

3.5. *Tracing Angular Momentum*

In moving from an inner disk or bulge-like component to an outer stellar halo we may expect changes in how much of the galaxy angular momentum is stored in random as opposed to ordered motion. With long-slit spectroscopy, typically only the ratio of maximum observed rotational velocity ($V_{\rm max}$) to central dispersion (σ_c; Illingworth 1977; Binney 1978b; Davies et al. 1983) can be measured. With IFS, which provides full 2D kinematic information, we can construct a more robust measure incorporating both radial and spatial variations. Binney (2005) introduced the ratio of the luminosity-weighted integrated quantites $\langle V^2 \rangle$ and $\langle \sigma^2 \rangle$. However, weighting by the surface brightness alone tends to overestimate the importance of central regions and conflate very different kinematic structures, such as organized rotation versus small central KDCs. To counteract this limitation, the SAURON survey introduced the parameter λ_R (Emsellem et al. 2007), which weights by radius as well as flux and therefore measures the projected baryonic specific angular momentum

$$\lambda_R \equiv \frac{\langle R\,|V|\rangle}{\langle R\sqrt{V^2+\sigma^2}\rangle} \qquad (3)$$

where the brackets indicate a flux-weighted sum within an ellipse of mean radius R. In calculating λ_R, we adopt the approach of Wu et al. (2014) and slightly modify the above definition. Instead of taking the absolute value of the velocity, we sum over the actual velocity separately on both sides of the rotation axis. This allows positive and negative noise terms to cancel, resulting in a smoother profile.

Errors on λ_R are estimated using the formal fit errors to V and σ. While systematic errors in the pPXF fits are likely an important factor, particularly in the inner regions (Emsellem et al. 2011), they will tend to have roughly the same effect on all galaxies. Therefore, these error estimates are at least indicative of the relative differences between galaxies.

Using λ_R, Emsellem et al. (2007) found that SRs and FRs could be quite robustly separated, with SRs being specified by $\lambda(R_e) \leq 0.1$ and FRs by $\lambda(R_e) \geq 0.1$. Emsellem et al. (2011) and Krajnovic et al. (2011), looking at the full ATLAS^{3D} sample, found that this simple picture was slightly blurred by inclination effects since a flattened system viewed face-on would have a similar profile to a nearly spherical galaxy seen at a large inclina-

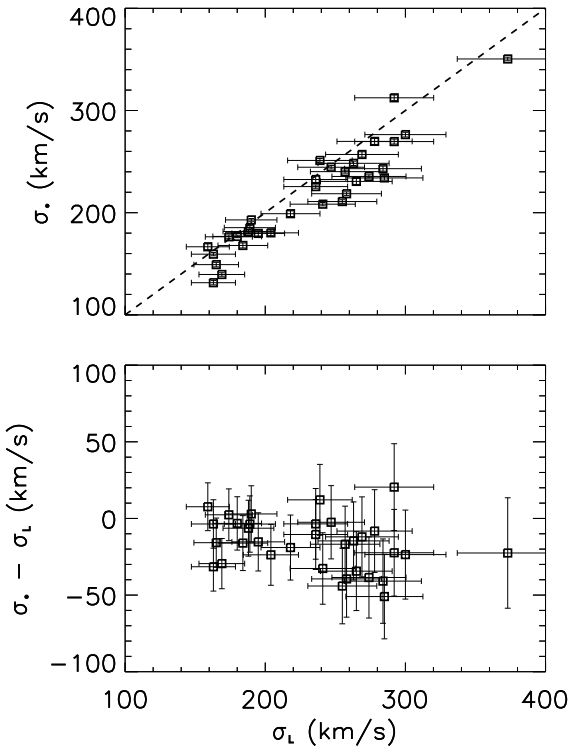

Figure 4. Velocity dispersions in the central fiber σ_c of our galaxies as compared with values taken from the literature $\sigma_{\rm L}$. We show both the dispersions themselves (top) and the offset between literature and our measurement (bottom). The literature values have been taken from the SDSS catalog (Blanton et al. 2005) as well as several collated data sets of galactic dispersions (Whitmore et al. 1985; McElroy 1998; Ho et al. 2009). The $\sim$20 km s^{-1} offset likely reflects our larger aperture, although our aperture does match relatively well to the SDSS.

tion angle. However, with a modified definition of FRs, $\lambda(R_e) \geq 0.31 \times \epsilon_e$, the same picture of two dichotomous families separated by their kinematics and formation processes still holds (e.g., Bender et al. 1989; Kormendy & Bender 1996; de Zeeuw 1985; Franx et al. 1991; de Zeeuw & Franx 1991; van den Bosch et al. 2008).

We calculate λ_R evaluated at the effective radius for each galaxy and classify them as slow (SRs) or fast rotators (FRs) based on the Emsellem et al. (2011) definition. Twenty-one of our galaxies are FRs, and the remaining 12 are SRs. As we will see below, there are some borderline cases, galaxies classified as FR that are right at the boundary within $\sim R_e$ but then do not rotate at all in their outer parts. Even sticking to the strict definition, we have a much higher percentage of SRs than the 14% found in the ATLAS$^{\rm 3D}$ sample. We also note that these classifications are entirely derived from the kinematics within R_e. In § 5.2 we will explore changes in λ_R with radius.

3.6. *Kinemetry*

Beyond just the angular momentum content with radius, we can also investigate different kinematic components in the galaxies. We turn to *kinemetry* (Krajnović et al. 2006) to help identify and characterize substructures in these maps. Kinemetry extends the basic assumption of photometry, that the surface brightness of ETG's is constant to within $\lesssim 1\%$ along best-fit ellipses, to higher order moments of the LOSVD. It assumes that symmetric (even) moments, such as the dispersion, are constant along ellipses while antisymmetric (odd) moments, such as the velocity, satisfy a simple cosine law to first order. Therefore, by fitting these kinematic parameters in elliptical annuli we may obtain simple radial profiles of the velocity and dispersion showing the scales at which important kinematic transitions occur.

In particular, application of kinemetry to our velocity maps allows us to derive radial profiles of the kinematic position angle $\rm PA_{kin}$ and flattening $q_{\rm kin}$ of our best-fit ellipses. We may furthermore decompose the velocity along these ellipses into Fourier coefficients

$$V(a,\phi) = V_0 + \sum_{n=1}^{\infty} A_n(a)\sin(n\phi) + B_n(a)\cos(n\phi) \quad (4)$$

where a is the ellipse radius and V_0 is the systemic velocity, set to a constant across all radii. The simple cosine law decomposition is dominated by the first order term, $k_1 = \sqrt{A_1^2 + B_1^2}$, which captures the rotation curve. By choosing best-fit ellipses we effectively minimise all higher order terms up to k_5. Radial profiles of these coefficients therefore also provide information on the rotation curve (k_1) and any deviations from the assumption of ellipticity (k_5), which tend to occur in transitions between components rotating at different velocities and/or PA.

This kinemetric analysis is essentially identical to that performed for the SAURON galaxies in Krajnović et al. (2008) and the ATLAS$^{\rm 3D}$ sample in Krajnovic et al. (2011), but because our data are so different we uncover different kinds of structures. Our galaxies have on average about 40 binned data points out to $\sim 3-4R_e$ compared to the thousands of points available to ATLAS$^{\rm 3D}$ galaxies within R_e. We cannot resolve classic kinematically decoupled components but we cover much larger-scale features.

Our sample characteristics are also different; a large fraction display little-to-no net rotation. These galaxies must be treated differently, since the determination of best-fitting ellipses for a velocity map close to zero everywhere is highly degenerate. Therefore, for cases where we have very low velocities $k_1 < 15$ km s^{-1}, we follow the approach of Krajnović et al. (2008) and rerun the kinemetric analysis assuming $q_{\rm kin} = 1$ (where q is the axis ratio). Deviations from a cosine profile, seen in the k_5 term, will be artificially inflated since a circular profile does not necessarily match the isovelocity contours and the $\rm PA_{kin}$ is poorly defined. However, they both provide some indication of the extent of the non-rotating component.

A final caveat is that our S/N, particularly at large radius, tends to be lower than for the ATLAS$^{\rm 3D}$ galaxies. For instance, whereas the average error on k_5/k_1 for the SAURON sample is 0.015 (Krajnović et al. 2008), our galaxies typically have errors in this ratio that approach 0.04. This means that as the S/N deteriorates, we are only sensitive to relatively large changes in $\rm PA_{kin}$, $q_{\rm kin}$

and k_5/k_1, around 10°, 0.2 and 0.1 respectively.

Nevertheless, with these caveats in mind, we may attempt to identify kinematic substructures on each map using a similar classification scheme to Krajnović et al. (2008) but with more conservative limits. In particular, we first differentiate between galaxies that are

1. Single Component (SC): Constant or slowly varying PA and q, with changes in the former restricted to less than 10°. We do not constrain q well enough to take changes in q alone as signs of a transition between components.

2. Multiple Component (MC): Abrupt change in ΔPA $> 10°$, or a double hump in k_1 with a corresponding local minimum or peak in k_5 with $k_5/k_1 > 0.05$

Individual subcomponents of each galaxy can then be identified as

1. Disk-like Rotation (DR): $k_5/k_1 < 0.05$, while variation in PA is less than 10°.

2. Low-level Velocity (LV): Maximum of k_1 is less than 15 km s^{-1}.

3. Kinematic Twist (KT): Smooth variation in PA of more than 10°.

4. Kinematically Distinct (KD) components: Abrupt change of larger than 20° between adjacent components or an outer LV component in which the derivation of PA is uncertain. Note we will not call these "kinematically decoupled cores" because we are only sensitive to structures larger than one kpc, while classic KDs can have scales of 100s of pc (Kormendy 1984; Forbes et al. 1994; Carollo et al. 1997). They are however quite similar in scale to the "kinematically distinct haloes" discussed in Foster et al. (2013).

We will classify each galaxy and discuss the characteristics of the different subclasses in § 4.

4. RESULTS: LOS KINEMATICS AT LARGE RADIUS

4.1. *Angular Momentum Classification*

Full 2D profiles of the velocity and velocity dispersion of all galaxies, as well as 1D kinemetric profiles, can be found in Figures B.1-B.6 of Appendix B. In addition, some key kinematic characteristics out to large radius are listed in Table 2. We include the traditional measures of maximum velocity, the dispersion within an effective radius, and the kinematic position angle. In addition, as we are largely interested in the evolution of kinematic properties at large radius, we include the radius of our maximum robust measurement and the dispersion at this radius.

For almost all galaxies our observations extend to beyond 2 R_e, or around 8 kpc. The only exception is NGC 1286, which has a relatively low dispersion and large R_e, as well as two nearby sources that contaminate our outermost bin and force us to discard it. For six galaxies, we are able to observe to $\gtrsim 5$ R_e (close to 20 kpc), although with wide bins ($\sim R_e$). Even accounting for our small R_e estimates, we probe the stellar kinematics out to distances well beyond most existing samples.

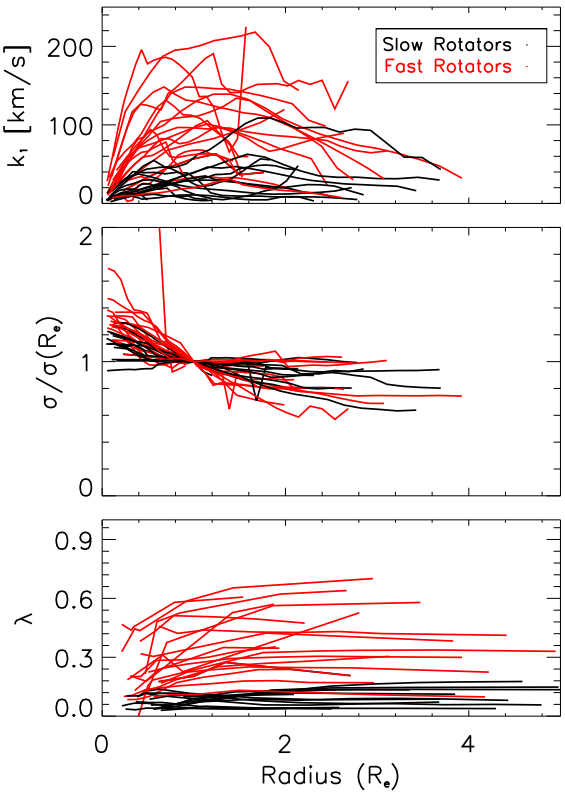

Figure 5. Velocity, dispersion and angular momentum profiles for all galaxies in our sample based on kinemetry. We show the first order harmonic velocity term k_1 (top), the velocity dispersion in elliptical annuli (middle), and the cumulative measure λ_R as a function of radius (bottom) for both SRs (Black) and FRs (Red).

In Figure 5, we show the velocity, velocity dispersion, and λ_R profiles for all galaxies. In general, we find that σ is declining gently ($\sim$ 23% per decade in radius on average), as has been observed many times at smaller radius (e.g., Jorgensen et al. 1997), and has also been reproduced in simulations (e.g., Remus et al. 2013; Wu et al. 2014). While some galaxies appear to show rising dispersion profiles at large radius, most are consistent with remaining flat beyond R_e within the measurement uncertainties. However, the two most massive galaxies in our sample, NGC 677 and UGC 4051, do show significant, albeit small ($\sim$ 5% above σ_{R_e}) rises in dispersion. The velocity dispersion profiles also appear to show a rough split between FRs and SRs. Most SRs have comparatively flat dispersions, particularly within R_e. By contrast, FRs tend to show more rapidly declining dispersion profiles out to R_e.

Given the integral nature of λ_R, in most cases galaxies reach a limiting value of λ_R at $1-2$ R_e. In this large radius limit, most SRs have $\lambda_R \lesssim 0.1$, while most FRs occupy a much broader continuum above $\lambda_R \sim 0.2$. Classifications based on kinematics within R_e are therefore quite accurate out to much larger radii. The main exceptions are the galaxies NGC 677, IC 301 and NGC 3837, which are classified as FRs based on $\lambda(R_e)$, but at large

Table 2
Kinematic Properties of the Galaxy Sample

Galaxy	$V_{\rm m}$	$R_{\rm max}$	$\sigma(R_e)$	$\sigma(R_{\rm m})$	$\lambda(R_e)$	$\lambda(R_{\rm m})$	Rot	Structure	R_t	Ψ
(1)	(2)	(3)	(4)	(5)	(6)	(7)	(8)	(9)	(10)	(11)
NGC 219	76.5 ± 5.7	1.42 - 2.87	159 ± 11	154 ± 15	0.20	0.21	FR	SC (KT)	—	27 ± 25
NGC 426	213.6 ± 5.7	2.35 - 3.23	166.7 ± 3.6	121 ± 41	0.54	0.64	FR	SC (DR)	—	-10 ± 12
NGC 474	50.0 ± 3.0	2.50 - 3.29	125.7 ± 2.4	98.1 ± 7.4	0.16	0.17	FR	MC (KD/DR, DR)	2.2	-3 ± 29
CGCG 390-096	99.2 ± 4.5	1.91 - 4.11	159.5 ± 2.7	151 ± 12	0.35	0.38	FR	SC (DR)	—	53 ± 34
NGC 661	67.1 ± 5.3	2.13 - 2.57	143.2 ± 3.1	92 ± 14	0.19	0.23	FR	MC (LV, DR)	1.9	3.0 ± 6.6
NGC 677	54.7 ± 3.8	4.57 - 5.14	209.4 ± 3.3	185 ± 19	0.11	0.057	FR	MC (KD/KT, DR)	4.3	0 ± 11
UGC 1382	104.4 ± 6.7	1.53 - 2.23	153.1 ± 2.9	167 ± 16	0.30	0.35	FR	SC (KT)	—	25 ± 40
NGC 774	141.2 ± 5.4	1.91 - 2.53	115.4 ± 2.4	130 ± 24	0.51	0.47	FR	SC (DR)	—	-2 ± 24
IC 301	32.7 ± 5.7	2.52 - 4.13	151.3 ± 3.3	81 ± 51	0.089	0.072	FR	MC (KD/DR, LV)	2.6	7.4 ± 8.3
NGC 1286	77.7 ± 3.6	1.58 - 2.08	63.0 ± 2.5	—*	0.37	0.57	FR	SC (DR)	—	-2 ± 34
IC312	199.7 ± 5.1	1.11 - 2.15	152.8 ± 5.3	141 ± 10	0.59	0.61	FR	SC (DR)	—	-43 ± 22
NGC 1267	64.4 ± 9.8	3.65 - 5.41	211.7 ± 7.8	196 ± 29	0.067	0.15	SR	MC (KT, DR)	3.8	35.9 ± 4.9
NGC 1270	145.7 ± 2.8	4.09 - 5.53	233.7 ± 1.7	183 ± 48	0.24	0.33	FR	SC (DR)	—	-28 ± 42
NVSS	103.4 ± 3.7	1.97 - 3.10	167.0 ± 3.6	112 ± 27	0.24	0.53	FR	SC (DR)	—	-28 ± 32
UGC 4051	135 ± 14	3.01 - 4.69	244.4 ± 5.4	234 ± 16	0.23	0.22	FR	SC (DR)	—	15 ± 32
NGC 3837	40.9 ± 3.4	2.78 - 4.29	199.9 ± 2.6	143 ± 12	0.11	0.087	FR	MC (KD/KT, LV)	7.1	-42 ± 27
NGC 3842	24.5 ± 5.8	2.13 - 2.77	219.6 ± 2.9	216 ± 13	0.039	0.037	SR	MC (KD/DR, LV)	3.2	31 ± 40
NGC 4065	41 ± 11	2.04 - 2.83	244.7 ± 4.3	218 ± 28	0.053	0.043	SR	MC (KD/KT, LV)	5.4	-4.8 ± 2.8
IC 834	143.5 ± 4.1	2.32 - 4.31	143.7 ± 5.0	119 ± 17	0.42	0.58	FR	MC (DR, DR)	3.2	-20.3 ± 3.4
NGC 4908	53 ± 17	1.64 - 2.52	254.4 ± 7.8	257 ± 49	0.11	0.11	SR	MC (KD/DR, LV)	5.7	-53 ± 33
NGC 4952	100.4 ± 7.6	2.74 - 3.91	213.0 ± 2.7	159 ± 15	0.21	0.30	FR	MC (DR, DR, DR)	3.1, 8.9	-1.3 ± 0.4
NGC 5080	57.7 ± 9.2	3.52 - 5.58	239.6 ± 4.9	146 ± 16	0.08	0.13	SR	MC (LV, DR)	2.6	-67 ± 47
NGC 5127	25.3 ± 4.7	1.90 - 2.36	162.5 ± 2.8	170 ± 16	0.041	0.038	SR	MC (KD/DR, LV)	4.7	73 ± 44
NGC 5423	101.2 ± 6.0	3.60 - 4.78	196.5 ± 3.6	225 ± 49	0.27	0.30	FR	SC (DR)	—	17 ± 26
NGC 5982	65.0 ± 9.8	3.34 - 4.01	206.7 ± 1.6	204 ± 9	0.076	0.13	SR	MC (LV, DR, DR)	1.6, 5.2	-10 ± 32
IC 1152	20.3 ± 6.0	3.61 - 4.71	181.9 ± 4.0	155 ± 16	0.043	0.038	SR	SC (LV)	—	-15 ± 27
IC 1153	155.5 ± 3.2	3.37 - 4.89	172.7 ± 2.9	104 ± 13	0.43	0.41	FR	SC (DR)	—	-1 ± 30
CGCG 137-019	34.2 ± 7.3	2.32 - 4.18	155.4 ± 3.0	114 ± 15	0.091	0.11	SR	MC (LV, DR)	2.4	23.5 ± 9.3
NGC 6125	38.8 ± 8.7	3.85 - 4.51	207.2 ± 3.2	204 ± 41	0.067	0.080	SR	MC (LV, DR)	4.9	16 ± 39
NGC 6482	114.8 ± 9.2	4.25 - 4.97	304.3 ± 4.2	225 ± 22	0.10	0.18	SR	MC (DR, DR)	1.6	51 ± 15
NGC 6964	99.9 ± 6.2	1.54 - 2.03	140.7 ± 4.5	88 ± 17	0.29	0.35	FR	MC (KT, DR)	4.0	27.5 ± 5.5
NGC 7509	41.3 ± 5.2	3.56 - 4.33	140.2 ± 3.0	148 ± 31	0.11	0.098	FR	MC (LV, DR)	3.6	-41 ± 36
NGC 7684	158.2 ± 4.7	1.97 - 4.07	114.3 ± 4.7	41 ± 22	0.60	0.70	FR	MC (KD/DR, DR)	4.0	-29 ± 17

Notes: Col. (1): Galaxy Name. Col. (2): Maximum rotational velocity measured as the maximum absolute deviation from the systematic recessional velocity. Col. (3): Maximum radius with robust kinematic results (in units of R_e). We show the minimum and maximum radius of the outermost spatial bin. Col. (4) Dispersion at the half-light radius. Col. (5) Dispersion at the maximum radius. *No measurement is possible for NGC 1286 as we are below the resolution limit. Col. (6): λ parameter at R_e as defined in Emsellem et al. (2007). Col. (7): λ parameter at $R_{\rm max}$ Col. (8): Classification as fast (FR) or slow (SR) rotator based on $\lambda(R_e)$ and the definitions in Cappellari et al. (2011). Col. (9): Structural Classification, based on Krajnović et al. (2008). The classes are DR (Disk-like Rotation), LV (Low-Level Velocity), KT (Kinematic Twist) and KD (Kinematically Distinct). Col. (10): Transition radius in kpc between first and second component, where relevant. Col. (11): Global Misalignment angle $\Psi = \langle {\rm PA_{kin}} - {\rm PA_{phot}} \rangle$ in degrees for the outermost component of each galaxy

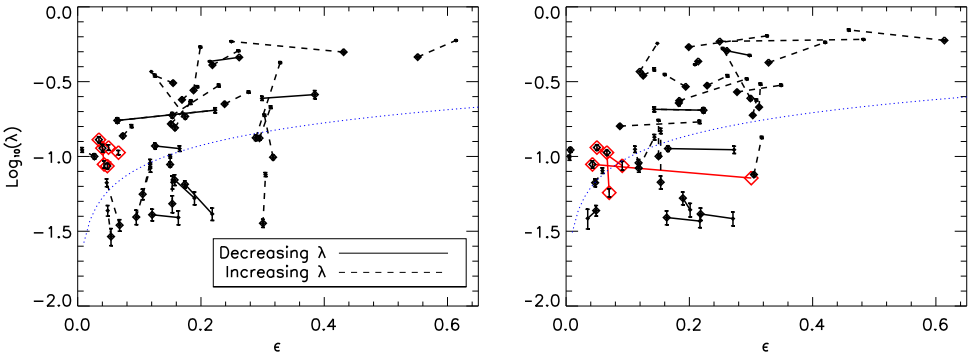

Figure 6. We show the cumulative measure λ_R as a function of ellipticity at both $R_e/2$ (left) and the outermost radius (right). In both cases, values at R_e are also plotted, with measurements at each radius connected by a solid line when λ_R increases outwards and a dashed line for decreasing λ_R. In a small number of cases, the ellipticity decreases moving outwards, leading to values of λ that decrease with radius, but increase with ϵ. For reference, the function $\lambda = 0.31\sqrt{\epsilon}$, which divides SRs and FRs, is overplotted (blue dotted line) though we note that the scaling of this function is radius-dependent. Galaxies NGC 677, IC 301 and NGC 3837, intermediate between SR and FR as discussed in the text, are shown with large diamonds. All three are low ellipticity galaxies with $\lambda(R_e) \sim 0.1$.

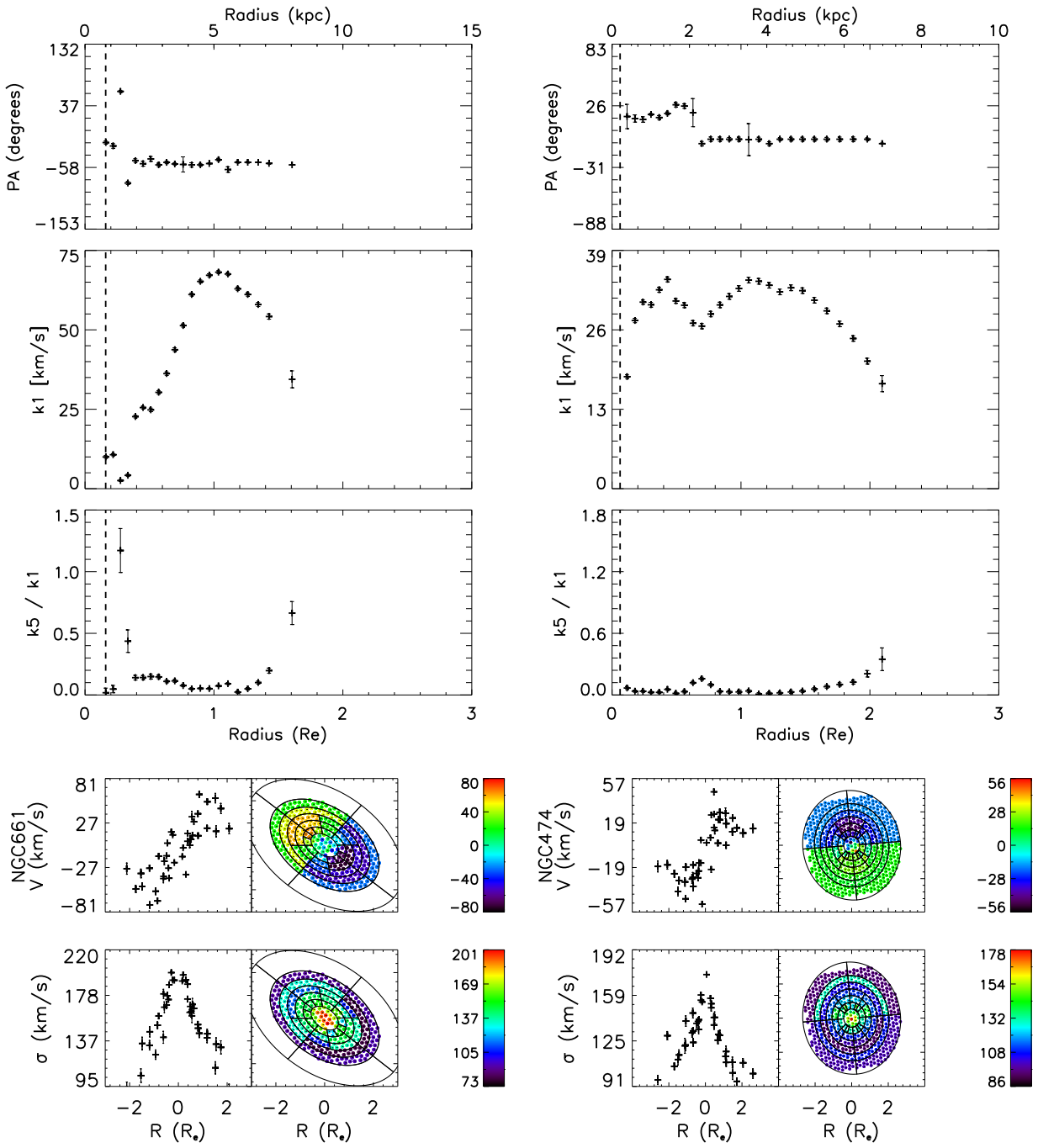

Figure 7. Kinematic and kinemetric maps for galaxies NGC 661 (left) and NGC 474 (right). In each case we show 1D radial kinemetric profiles including the PA (top), first coefficient in the harmonic dispersion expansion k_1 (the rotation curve; top middle) and k_5/k_1 (middle). Below are 2D maps of the velocity (bottom middle) and velocity dispersion (bottom) for each galaxy. NGC 661 is very similar to most of the SC FRs in our sample, with flat k_5/k_1 and PA, and a rotation profile that flattens or decreases slightly beyond $\sim R_e$. It also possesses a more pronounced LV region in its inner kpc, which we believe is characteristic of an unresolved KD component. NGC 661 is a more typical MC FR, with a clear transition between two disk-like components at 2 kpc.

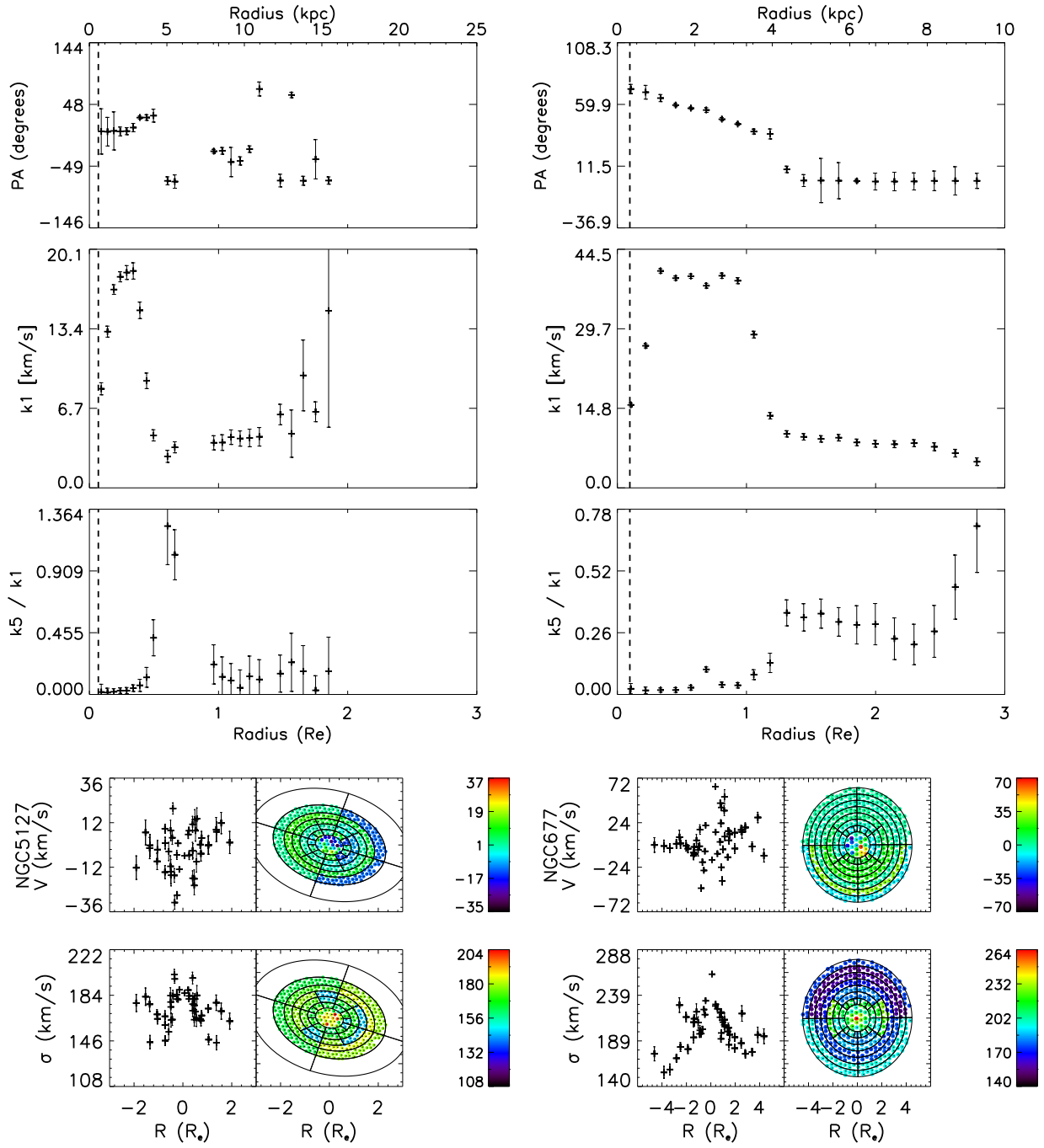

Figure 8. Identical to Figure 7 for galaxies NGC 5127 (left) and NGC 677 (right). NGC 5127 is a typical example of an SR with an extended disk-like KD component at its center. At 5 kpc, there is a sharp transition in PA, and a hump in k_5/k_1, as the galaxy transitions to an outer LV component. On the other hand, NGC 677 is an example of a galaxy classified as an FR based on $\lambda(R_e)$, but displaying all the same characteristics as NGC 5127. It is only the extended nature of the inner disk-like component that leads to its classification as an FR.

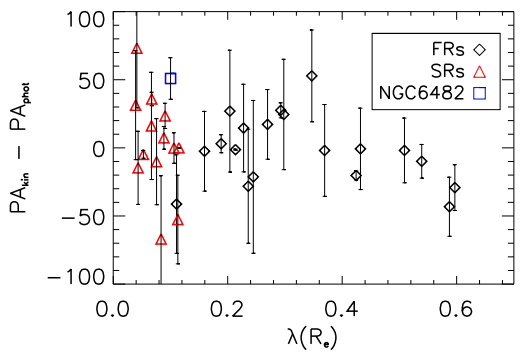

Figure 9. Global misalignment angle $\langle \mathrm{PA_{kin}} - \mathrm{PA_{phot}} \rangle$ as a function of $\lambda(R_e)$ for the outermost kinemetric component of all galaxies. $\mathrm{PA_{kin}}$ and $\mathrm{PA_{phot}}$ are both calculated in best-fit elliptical annuli and the average misalignment angle of this component is then found by taking a luminosity-weighted average over all radii in the region. We choose the outermost component to avoid LV regions at the centres of most galaxies where $\mathrm{PA_{kin}}$ is poorly defined, and typically cover between $\sim 0.5 - 2.5 R_e$. Error bars are the 1-σ standard deviations when we average over all radii. We observe a general trend of greater misalignment amongst SRs, including NGC 677, IC 301 and NGC 3837, and highlight NGC 6482 (blue), which has the largest well-defined misalignment.

radius show λ_R characteristic of minimal rotation.

This is also clear if we consider the behaviour of λ as a function of observed ellipticity (Binney 1978b). In Figure 6, we show galaxies on the $(\lambda - \epsilon)$ plane at $R_e/2$, R_e and R_{max}. Very few galaxies show significant changes in λ even beyond $R_e/2$. Almost all changes are restricted to increases in ordered rotation amongst FRs, which tend to continue rotating out to radii well beyond R_e. The only galaxies that show significant enough decreases to transition from fast rotation within R_e to slow rotation in their outskirts are the three galaxies identified in the previous paragraph, which uniformly also have higher ellipticity in their outskirts.

4.2. *Kinemetric Classification*

We now turn to identifying substructures based on kinemetry. We first classify each galaxy as single (SC) or multi-component (MC), and then classify each component as either disk-like rotation (DR), low velocity (LV), kinematic twist (KT) or kinematically decoupled (KD). 13 (40%) of our galaxies are SC systems, a slightly higher percentage than the 31% in the SAURON sample. We do not necessarily expect these numbers to align since the two samples cover different mass ranges and additionally, we are unable to resolve central structures with sizes $\lesssim 1$ kpc. Of the SCs, only one (IC 1152) is an SR, and the remaining 12 are SC FRs. Almost universally, the single component in these cases shows disk-like rotation and close to perfect alignment between kinematic and photometric PA. Furthermore, the λ_R profiles tend to be flat or rising for the SC FRs, as shown in Figure 5. There are one or two examples with small kinematic twisting (NGC 219 and UGC 1382), as well as two disk-like rotators (NVSS J032053+413629 and IC 312) that show strong kinematic misalignment in the sense that $\mathrm{PA_{kin}}$ deviates from the photometric PA by close to 90° at large radius.

Of the MC galaxies, 33% contain an LV component in the center with the rotation curve increasing outward. An additional 28% have a kinematic twist. The remaining 39% contain a KD ranging in size from 1-7 kpc. We now describe the properties of these subclasses.

There are ten MC FRs, which come in a few varieties. Three of them have disky kinematics everywhere except in a small LV region in the center. Two such examples of these, NGC 474 and NGC 661, are identified in Figure 7, which shows radial profiles of k_1, $\mathrm{PA_{kin}}$ and k_5/k_1 as well as 2D kinematic maps for these two galaxies. Very likely these rapid drops in velocity and λ_R point to small rotating components that are unresolved by our observations. In particular, our observations of NGC 474 and NGC 5982 show low velocities in their central fibers whereas higher resolution SAURON kinematics identify KDC's rotating at ~ 50 km s^{-1} within 1 kpc. The velocities also appear to drop in the outer parts of the FRs, but this is likely due to our large spatial and angular bins at large radius.

Another four of the MC FRs are typified by NGC 474, shown in the bottom panel of Figure 7. These relatively slowly rotating FRs contain two distinct disk-like components, in the case of NGC 474 separated by a PA shift of about 15° at 2 kpc. The transition is also marked by a clear hump in k_5 and a minimum of k_1. SAURON kinematics of NGC 474 also show an additional inner disk-like component at 0.8 kpc (Krajnović et al. 2008) that we do not detect, empirically determining that structures with sizes $< 7''$ are not discernible in our data.

There are three remaining MC FRs (NGC 677, shown in the top of Figure 8, NGC 3837 and IC 301), and these are the most difficult to classify. While technically they satisfy the FR criterion, their λ_R values are borderline between FRs and SRs, and they do not rotate at all beyond $\sim 1.5 - 2\ R_e$. From Figure 6, we see that all of these are low ellipticity galaxies, which never rotate particularly fast in the sense that $\lambda(R_e) \lesssim 0.15$. NGC 677 exemplifies this class. NGC 677 also has an interesting outer dispersion profile that appears to start to rise again at around 3 R_e (10 kpc) on both sides of the galaxy along the minor axis, as has been seen in a few central galaxies (see e.g. Dressler 1979; Kelson et al. 2002; Loubser et al. 2009; Jimmy et al. 2013; Murphy et al. 2013, for other examples of dispersion profiles rising outwards)

In fact, these three borderline cases have very similar kinemetric profiles to five of the MC SRs. Specifically, they all have a central component with low-amplitude rotation and large angular differences between photometric and kinematic PAs, which then transitions to an LV component at larger radius. NGC 5127, top left of Figure 7, is one good example. The three borderline cases were classified as FRs only because the scale of the inner rotating component is a bit larger than for the typical MC SRs. Therefore, while we technically count these three galaxies as FRs, perhaps they are better considered as SRs with a very extended KD in the center. These central KD components, with sizes of 2.2 to 7 kpc, are considerably larger in size than KDCs (0.2 to 1.8 kpc in SAURON Kormendy 1984; Forbes et al. 1994; Carollo et al. 1997; Krajnović et al. 2008), but are otherwise kinematically quite similar.

Finally, beyond the one SC SR, and the five MC SRs with KD components, we see one more type of MC SR, comprising five galaxies, that show steadily increasing λ_R profiles in Figure 5. As can be seen from Figure 6, none

of them increase their rotation enough to become FRs in their outskirts. All of the five galaxies, and particularly NGC 6482, also show evidence of misalignment between their photometric and kinematic PAs.

We see this in Figure 9, which plots the misalignment angle $\langle \mathrm{PA_{kin}} - \mathrm{PA_{phot}} \rangle$ of the outermost component in each galaxy, generally covering radii between $\sim 0.5 - 2.5 R_e$. Here, $\mathrm{PA_{kin}}$ and $\mathrm{PA_{phot}}$ are calculated independently in best-fit elliptical annuli, using kinemetry applied to our kinematic data and r-band photometry respectively. The average misalignment angle for a given galaxy or component is then found by taking a luminosity-weighted average over all radii in that component. Since we restrict our attention to the range $[-90°, 90°]$, this is comparable to the kinematic misalignment angle $\sin\Psi = |\sin \mathrm{PA_{kin}} - \mathrm{PA_{phot}}|$ defined by Franx et al. (1991). We choose to only show the outer component to avoid any strong luminosity bias towards central regions and to avoid the rapid transitions in $\mathrm{PA_{kin}}$ seen between different components.

In the FRs, $\mathrm{PA_{kin}}$ is well-defined, and in almost all cases is aligned with $\mathrm{PA_{phot}}$. It is more difficult to determine the situation for the SRs since they are nearly round and have poorly defined $\mathrm{PA_{phot}}$. However, the five MC SRs with increasing λ_R profiles have better defined and quite large misalignment angles. NGC 6482 specifically, highlighted in Figure 9, is misaligned by $\sim 60°$. Such misalignment is typically interpreted as evidence of triaxiality, since projection effects in triaxial galaxies can lead to observed differences between the angular momentum vector and the major axis (Statler 1991). Therefore, we suggest that at least half of our SR galaxies probably have triaxial structure. This fits in with the existing picture of SRs within R_e, which show signs, based on their photometry, of being mildly triaxial (Binney 1978a; Tremblay & Merritt 1995, 1996; Krajnović et al. 2008; Krajnovic et al. 2011).

5. DISCUSSION

5.1. *Expectations for Large Radius Kinematics*

Before we examine the kinematics of our galaxy sample at large radii, we begin by reviewing the possible formation paths for ETG's and the results we may expect from any given formation scenario. The so-called two-phase picture of elliptical galaxy formation (van der Wel et al. 2008; Naab et al. 2009; Oser et al. 2010; Khochfar et al. 2011; van de Sande et al. 2013) posits that the central $\sim 1 - 5$ kpc of galaxies are initially formed by a fast, dissipational phase, which leaves behind a compact stellar disk with relatively high rotational support $\lambda \sim 0.5$ (Elmegreen 2009; Dekel et al. 2009; Ceverino et al. 2010; Khochfar et al. 2011). At later times dry merging expands the galaxy's outskirts in a manner that reduces λ and leaves behind rounder and kinematically hotter remnants (e.g., Naab et al. 2009; Hilz et al. 2013; Taranu et al. 2013).

The two-phase picture predicts that ETG's are inherently multi-component systems, with rotationally supported disks comprised primarily of in situ stars at their center and much rounder halos made up of accreted material. However, observations at large radius remain limited. While KDCs on small scales are interpreted as evidence of prior dissipational merging, most observed ETG's are FRs for which no evidence of such transition has been found, e.g., by ATLAS^{3D}.

We thus focus on the MC galaxies discussed in Section 4 and whether or not the transitions we observe beyond R_e fit into the two-phase formation picture. We consider kinemetric transitions between rotation-supported and dispersion-supported regions, how similar they are to the KDCs of Krajnovic et al. (2011) and whether they are accompanied by any similar transitions in λ_R. Finally, we consider the stellar populations associated with each subgroup, and whether they are characteristic of a move from in situ to accreted stars.

We are also interested in comparing to the picture presented by Arnold et al. (2013), who were able to use the SLUGGS survey to measure kinematics out to $\sim 5\ R_e$. They reported falling profiles in local angular momentum, perhaps reflecting transitions in some FRs from an inner disk to an outer halo at ~ 5 kpc, most dramatically in NGC 3377. They also found that S0s with more extended disks are most likely to show rising λ profiles at large radius while elliptical galaxies are most likely to have falling λ profiles. Finally they reported signs of PA alignment between inner disk and outer halo. Together these were used to argue for the two-phase picture and against the formation of disks by late-time major mergers (Hoffman et al. 2009), since 1:1 mergers result in significant kinematic decoupling between the inner disk and outer halo (Hoffman et al. 2010). However, we note that Naab et al. (2013) present a more nuanced view of the origin of SRs and FRs, in which either class can emerge from either a recent major merger, or a series of minor mergers, depending on the fraction of in-situ star formation and gas-richness of the last major merger.

We also compare with the simulations of Wu et al. (2014). This work derives galaxy kinematics at large radii from cosmological simulations of galaxy formation. They focus on a lower-mass sample (stellar masses of $\sim 3 - 5 \times 10^{10} M_\odot$ compared to our $\sim 2 - 20 \times 10^{10} M_\odot$) with kinematics that extend out to $\sim 6\ R_e$. However, they present simulated rotation and angular momentum profiles that correspond quite well with our observations.

5.2. *Galaxies with Changing Kinematics*

In order to emphasize radial changes, Arnold et al. (2013) consider a spatially varying specific angular momentum Λ, defined in elliptical annuli rather than full elliptical apertures. Since a local determination largely removes the effect of radial weighting, Λ is very similar to the flux-weighted ratio of velocity to dispersion, $\langle V^2 \rangle / \langle \sigma^2 \rangle$ used by Binney (2005) and Wu et al. (2014). Our elliptical annuli in the central regions are calculated using $5''$ windows, and outside of this region are aligned with our previously described spatial bins. Additionally, instead of flux-weighting, which does not vary much in each elliptical bin, we weight by the measurement errors. Since S/N is correlated with flux, the two methods do not differ much, but our approach is more robust to outlying measurements.

Figure 10 shows rotation curves (k_1), normalized velocity dispersions, and Λ profiles for galaxies split into SRs and FRs. To highlight the different kinematic transitions observed, we further subdivide our sample into SC systems, MC galaxies with KD's, and other MC galaxies. In all cases, the local measure Λ naturally shows

much greater variation than λ out to large radius. Partly this is due to the lower quality spectra in these regions, which means that errors increase outwards, rather than decreasing as in the cumulative case. However, we truncate the Λ profiles where the errors exceed ± 0.025, while the changes we observe in Λ are larger than this, and thus likely real.

5.2.1. *FRs at Large Radius*

For FRs, the distribution of Λ looks qualitatively similar to the 22 galaxies observed by the SLUGGS survey and the numerical results of Wu et al. (2014). In higher mass FRs, Λ tends to decline slightly or remain flat, while the majority of the FRs with lower mass tend to have rising Λ profiles. Since we can only reach $\sim 2R_e$ in these lower-mass galaxies, it is possible that we simply have not reached a large enough radius to see the Λ profile flatten/fall.

The galaxies with declining Λ profiles are predominantly SC disk-like FRs, as can be seen from the left-most panel of Figure 10. This subset includes the galaxies with the sharpest declines in Λ: NGC 774 at low mass and UGC 4051 at high mass, both of which have $\delta\Lambda \sim 0.1 - 0.2$. These SC FRs also almost all show a decline in the rotation curve beyond $\sim R_e$, which is typically accompanied by increases in k_5/k_1 to ~ 0.3. The declining S/N and large spatial bins also contribute to the large k_5/k_1 values. However, given the rough correspondence between drops in Λ and k_1, both of which are calculated independently, it seems unlikely that S/N alone is behind the radial changes.

We now ask whether these galaxies are showing signs of the transition from inner disk to outer halo detected by Arnold et al. (2013). As mentioned earlier, none show nearly as rapid a decline in Λ as that seen in NGC 3377, so it is not clear on a galaxy-by-galaxy basis that we are seeing this transition. However, statistically, we may ask whether we see the correlation between angular momentum gradients and Hubble Type seen by Arnold et al. (2013). In Figure 11 we show the radial variations in Λ between $R_{\rm max}$ and R_e (top) and also between R_e and $0.5R_e$ (bottom) for all FRs as a function of the Hubble Type and of $\lambda(R_e)$. In this case, we omit the two galaxies with $R_{\rm max} \lesssim 2R_e$ as these lack sufficient data for a robust measurement of $\Lambda(> R_e)$. We also show the corresponding measurements for the SLUGGS, and where possible, ATLAS^{3D}, surveys. The former are taken directly from Arnold et al. (2013), while for the ATLAS^{3D} survey, values of Λ within R_e are calculated from the full 2D stellar kinematics. In both cases, Hubble types are taken from the HyperLeda[4] database (Paturel et al. 2003).

As described in Arnold et al. (2013), the fastest declining SLUGGS galaxies tend to be elliptical, while most of those that rotate more outwards are S0's. However, we do not notice any such trend for our sample. If anything the reverse holds true, with our S0s having the fastest declining Λ profiles while the ellipticals show the largest Λ increases. Hubble type is not a continuous quantity, but if we naively fit lines to the radial gradient $\Lambda(R_{\rm max}) - \Lambda(R_e)$ as a function of T, then we obtain a positive Pearson correlation coefficient of $r = 0.45$ ($p = 0.036$) for the SLUGGS sample as opposed to $r = -0.18$ ($p = 0.32$) for ours and $r = -0.01$ ($p = 0.94$) for the joint sample. This seems to point to a lack of correlation between declining Λ and disky galaxies.

We lack the statistical significance to make any strong statement about correlations between morphology and large scale kinematics. However, as an interesting exercise, we may ask the same question of the entire ATLAS^{3D} sample, as shown in the top right panel of Figure 11. Naturally, in this case we are restricted to $< R_e$, but even within this smaller aperture, we already see gradients comparable to, or exceeding, the changes out to $\sim 4R_e$. Equally, within this much larger sample, we see no evidence of any difference in Λ gradients between the E and S0 galaxies, and a simple fit gives a correlation coefficient of $r = 0.01$, entirely consistent with zero.

As a final comparison between the two samples, we may consider the kinematics and morphology of our fastest declining FR, UGC 4051. Figure 12 shows the velocity and dispersion maps for this galaxy. If there were an embedded disk we may expect that along the major axis, where the disk is located, there would be lower velocity dispersion with respect to the minor axis, which contains mostly halo stars. We see no such evidence of such a feature. Kinematic maps of other rapidly declining galaxies (particularly NGC 774) also show no such behaviour, although this effect may only be pronounced if the galaxy were edge-on. Given also our low kinematic resolution this does not necessarily preclude the presence of stellar disks in these systems.

There are a number of key differences between our sample and SLUGGS that may explain the differences in our results. Firstly from a methodological perspective, our galaxies are binned at much lower spatial resolution, particularly at large radius. However, it seems unlikely that this could explain our dearth of galaxies with pronounced declines in Λ as compared to SLUGGS. If anything, averaging over large spatial bins would tend to artificially lower the measured velocity and thus also Λ.

More physically, our sample covers more massive galaxies, which may tend to have smaller Λ gradients. For instance, the simulated galaxies in Wu et al. (2014) show a trend with stellar mass, in the sense that the low-mass FRs are more likely to show declining Λ profiles. Perhaps we need to probe even larger radii to see the transition to a halo component in these more massive galaxies. Thus, our differences with the SLUGGS sample may be simply explained by the bias towards higher mass in our sample.

5.2.2. *SRs at Large Radius*

For at least half the SRs, the picture is comparatively simple. Aside from the completely non-rotating SC SR IC 1152, five SRs show central kinematically decoupled components characteristic of a transition from an inner disky structure to an outer halo. The decoupled components seem to be similar to the KDCs described in Krajnovic et al. (2011), which were interpreted as remnants of old, wet, major mergers.

If these kinematic transitions actually signal a component with a different formation history, then we could be seeing the remnant of an early dissipational component transitioning to an outer halo (Arnold et al. 2013). On the other hand, these components are large (1-7 kpc)

[4] http://leda.univ-lyon1.fr.

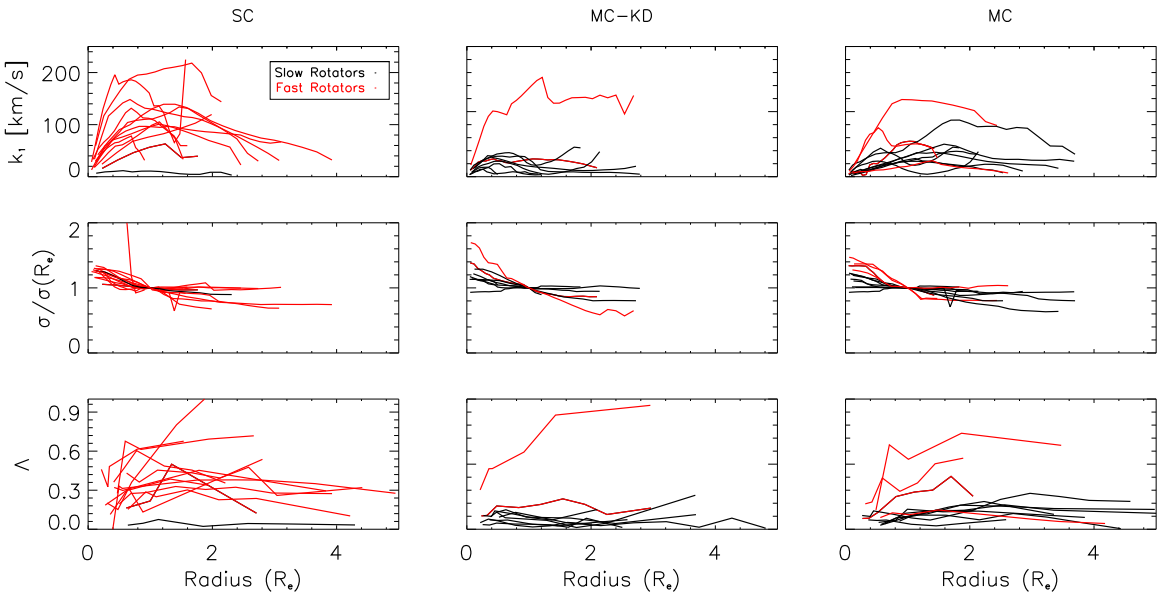

Figure 10. Velocity, normalized velocity dispersion and angular momentum profiles for all galaxies in our sample. We show the first order harmonic velocity term k_1 (the rotation curve, top), the velocity dispersion in elliptical annuli (middle), and the local measure of angular momentum, Λ_R as a function of radius (bottom) for both SRs (Black) and FRs (Red). Results are additionally divided into SC galaxies (left), MC galaxies with KD's (middle) and other MC galaxies (right). For simplicity, we classify the 3 galaxies NGC 677, IC 301 and NGC 3837 as SRs with KDs, since their kinematic behaviour is most similar to this class.

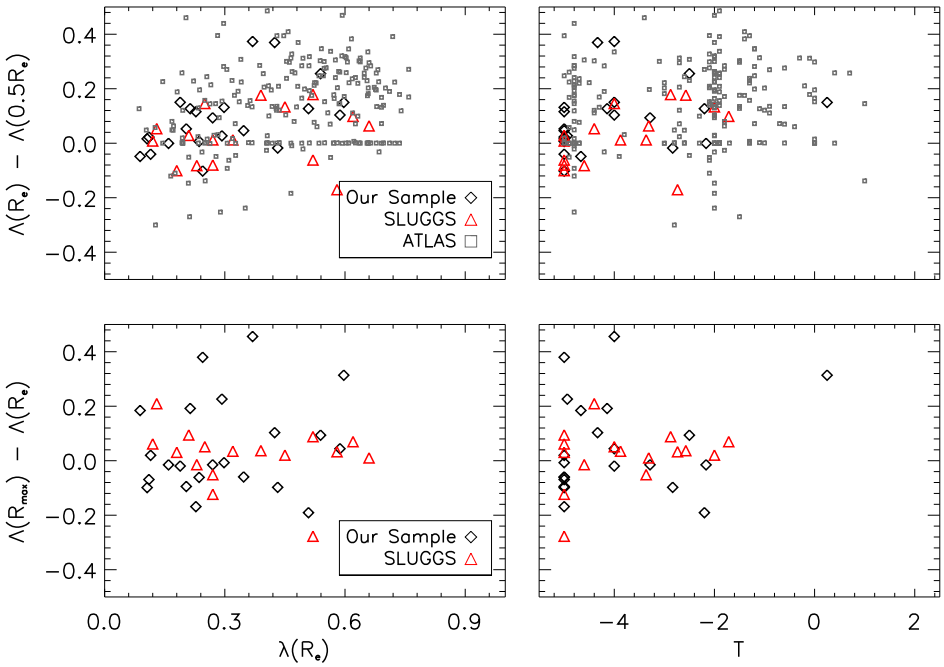

Figure 11. Radial gradient in the angular momentum between R_e and $0.5R_e$ (top) and the outermost measured radius $R_{\rm max}$ and R_e (bottom). We show the gradient vs. both $\lambda(R_e)$ and the morphological T-type number, where $T > -3.5$ indicates a lenticular galaxy. In all cases, we show only FRs from our sample (black diamonds), SLUGGS (red triangles) and where appropriate ATLAS^{3D} (grey squares). The ATLAS^{3D} values were calculated from their published stellar kinematics, while for SLUGGS, the relevant values were drawn from Arnold et al. (2013). For the ATLAS^{3D} sample, the large subset of galaxies clustered around zero gradient arises from those galaxies observed with relatively small apertures.

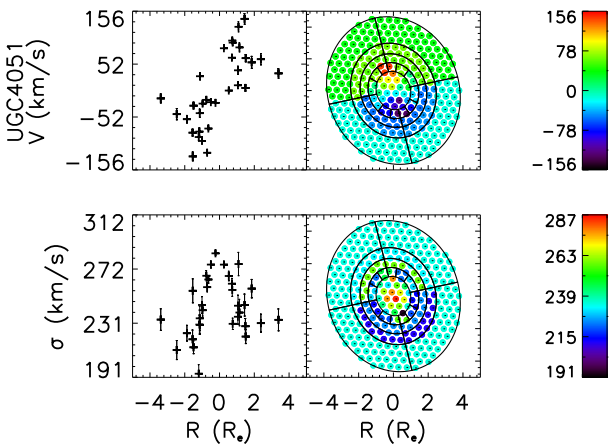

Figure 12. 2D velocity (Top) and dispersion (Bottom) maps for UGC 4051.

and have low amplitude rotation ($\Lambda \lesssim 0.2$ as compared to $\Lambda \sim 0.6$). Furthermore, the kinematic and photometric position angles are generally misaligned. For all of these reasons, we believe we are instead seeing signs of triaxiality (e.g., Statler 1991). This triaxiality also likes results from merging, as pointed out for NGC 5982 by Oosterloo et al. (1994). In fact, simulations suggest that triaxiality is strongly correlated with the box orbits that result from specifically dry major mergers (Jesseit et al. 2005, 2007; Hoffman et al. 2009).

In the same way, we have argued that the SRs with rising Λ profiles also show clear signs of triaxiality (as typified by NGC 5982 and NGC 6482). They generally show some evidence of a central LV component that transitions to slow disk-like rotation. In addition, the PA tends to be misaligned with the photometric axis in the central regions. NGC 6482 particularly shows strong kinematic misalignment of between 20° and 50° out to at least $\sim 2R_e$. Based on their complicated kinematics, both galaxies have been put forward as recent merger remnants (Statler 1991; Oosterloo et al. 1994; Del Burgo et al. 2008). While more detailed comparisons are needed, it seems likely from simulations that a series of minor mergers are needed to reproduce both the low λ and generic triaxial properties of the MC SRs (e.g., Bois et al. 2011).

5.3. *Correlations with Stellar Populations*

We now ask whether there are any differences in the stellar populations of our sample as a function of λ. For instance, if high λ is a signpost of dissipational formation, we might expect younger, more metal-rich stellar populations in the outer parts of FRs. Following Greene et al. (2013), we construct composite spectra as a function of radius, dividing the sample into FRs and SRs. To try and mitigate the strong impact of σ, we restrict our attention to galaxies with central stellar velocity dispersion σ_c, as measured by the SDSS, greater than 200 km s^{-1}. There are 10 SRs and 12 FRs included in our stacked spectra.

We construct composite spectra as described in Greene et al. (2013). In brief, we first substract emission-lines iteratively using continuum fits (e.g., Graves et al. 2007). Then, we divide each spectrum by a heavily smoothed version of itself to remove the continuum, and combine them using the biweight estimator (Beers et al. 1990). We then measure the Lick indices, and invert them to infer the ages, metallicities, and abundance ratios at each radial bin for the SRs and FRs, using *EZ_Ages* (Graves & Schiavon 2008). In addition to stellar age, [Fe/H], and [α/Fe] abundance ratios, the code also iteratively solves for the [C/Fe] and [N/Fe] abundance ratios, the former based mostly on the C_2 λ4668 Swann band, and the latter on the blue CN bands.

We note that the absolute values of [C/Fe] and [N/Fe] are uncertain because they depend directly on the oxygen abundance. Oxygen, as the most abundant heavy element, has a large indirect impact on the spectra but as there are no broad-band O indices, we must assume a value for [O/Fe]. Here we assume that it tracks the other α elements. Because the C gets bound up in CO molecules, the assumed oxygen abundance has a significant effect on the modeled [C/Fe] and therefore [N/Fe] (Graves et al. 2007; Greene et al. 2013). Specifically, if we lowered the assumed [O/Fe] to a solar value, the [C/Fe] and the [N/Fe] would fall, while their relative trend is robust (see discussion in Greene et al. 2013).

The radial profiles of our measured stellar population properties are shown in Figure 13. There are no significant differences between SRs and FRs. However, there are some intriguing hints. First of all, the FRs appear to have a slight tendency to get older in the outermost bins. In fact, we see a weak trend for positive age gradients as well when we consider individual galaxies, but it is not statistically significant. If true, we may be seeing the transition from stellar disk to stellar halo in the FRs. Over the past year, we have gathered data for twice as many galaxies, which will allow us to bin in both σ_c and λ.

We are left with a slightly ambiguous picture of how our galaxy sample ties into two-phase galaxy formation. Our observed FRs may show signs of a transition from inner disk to outer halo through small drops in the net rotation. However, these are typically not accompanied by the significant drops in angular momentum reported in Arnold et al. (2013) or any significant change in stellar populations. Nor are the observed drops in angular momentum correlated with E galaxies, as we might expect if S0's were characterised by more extended disks. Perhaps this is entirely a function of mass, since simulations of two-phase galaxy assembly by Wu et al. (2014), with which our observations seem to agree quite well, show fewer angular momentum transitions as we move to higher mass.

6. SUMMARY AND FUTURE WORK

We have presented wide-field 2D kinematic LOSVD's (out to radii between 2 and 5 R_e) for a sample of 33 massive elliptical galaxies previously described in Greene et al. (2013). Our sample comprises 12 Slow (SRs) and 21 Fast Rotators (FRs), with classifications based on kinematic information out to R_e. By design, this is a higher fraction of SRs than the volume-limited ATLAS^{3D} and SLUGGS samples.

Despite covering a broad range of central dispersions, sizes and environments, we find that most of the galaxies can be well classified on the basis of their kinematic and kinemetric information. A majority of the FRs are

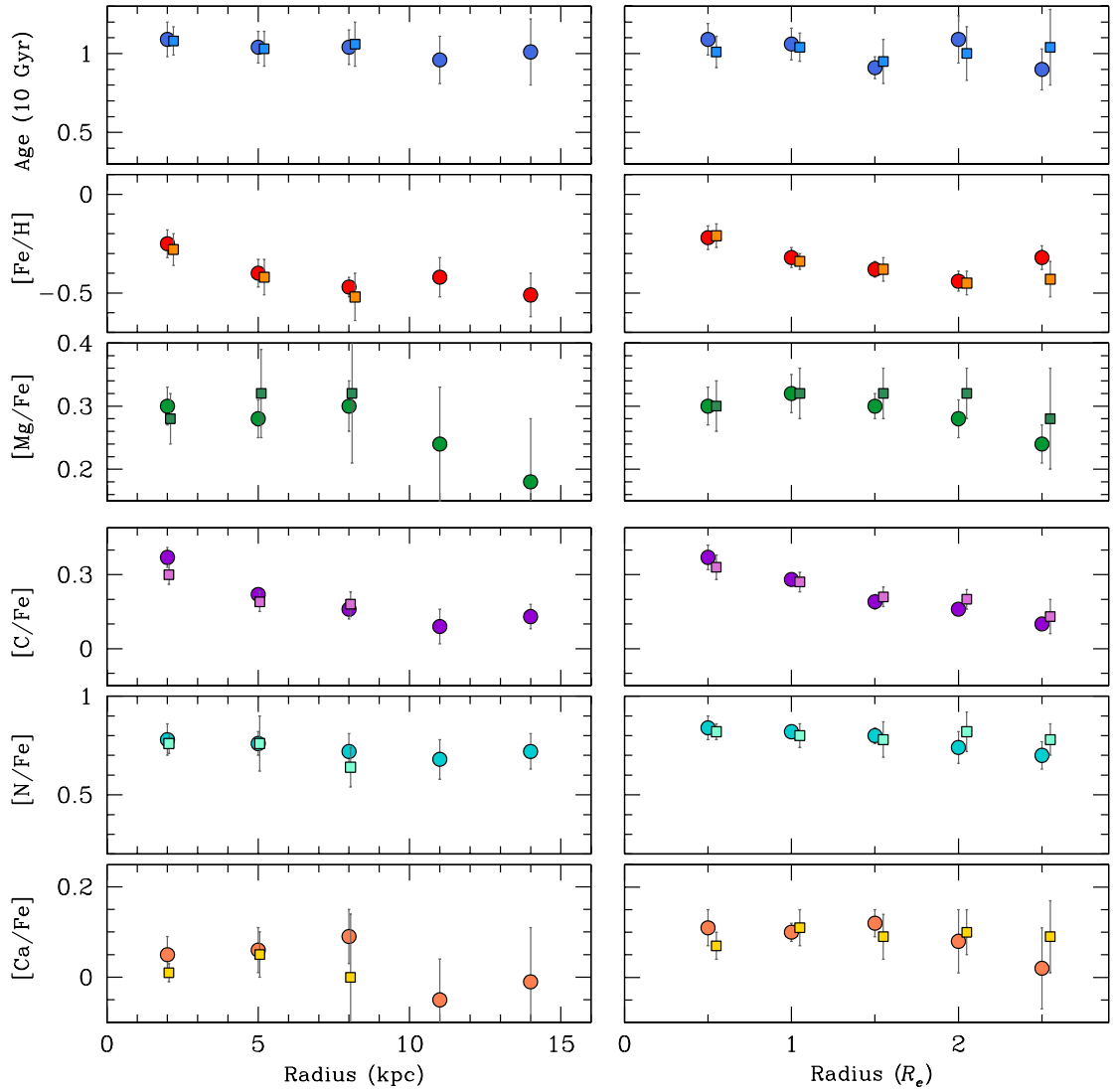

Figure 13. Radial gradients in age, [Fe/H], [Mg/Fe], [C/Fe], [N/Fe], and [Ca/Fe] as calculated by *EZ_Ages* from the Lick indices measured in the composite spectra. We show both the measurements for SR (circles) and FR (squares) galaxies as a function of R in kpc (left) or R/R_e (right).

single component disk-like rotators, with any decoupled components usually being in the form of central low velocity regions that likely signal unresolved rotation. They do show some tentative indications of transitioning from stellar disk to halo beyond R_e, but we observe no galaxies with the dramatic drops in angular momentum reported in Arnold et al. (2013). Generally, our FR galaxies continue rotating as far out as we observe. A majority of the SRs meanwhile show kinematically distinct components with disk-like properties at their centre, but these typically rotate more slowly and are much larger than the KDCs found in SAURON.

Our work, along with SLUGGS, represents an early effort to classify the outer parts of massive elliptical galaxies based on their kinematic properties. If we interpret the ubiquitous multi-component nature of the SRs as evidence for different formation histories, then we see some evidence for an "inner" and "outer" component, with a transition ~ 5 kpc. However, without more concrete comparisons with theory, it is hard to say whether we are seeing different phases of elliptical galaxy growth, or just triaxial galaxies in projection.

Furthermore, many of the trends we observe are relatively uncertain due to the small size, and incomplete selection, of our sample. We are currently in the process of doubling our sample, which combined with more detailed dynamical modelling of our galaxies, should be able to provide more insight into elliptical galaxy formation and particularly two-phase assembly. Specifically, dynamical studies, which reveal the DM fraction, velocity anisotropy and gravitational potential, should, in combination with stellar population results, be able to constrain both when and where outer halo stars were assembled. By offering a more direct comparison with cosmological-scale simulations of elliptical galaxy formation, we may then be able to comment more conclusively on exactly when and how the most massive galaxies were formed.

We would like to thank the referee for a prompt and

helpful review. We also thank D. Krajnovic, A. Romanowky, and J. Brodie for their feedback, which substantially improved this manuscript. We acknowledge the usage of the HyperLeda database (http://leda.univ-lyon1.fr)

REFERENCES

Adams, J. J., Gebhardt, K., Blanc, G. A., et al. 2012, The Astrophysical Journal, 745, 92
Adams, J. J., Blanc, G. A., Hill, G. J., et al. 2011, The Astrophysical Journal Supplement, 192, 5
Arnold, J. A., Romanowsky, A. J., Brodie, J. P., et al. 2011, The Astrophysical Journal Letters, 736, L26
Arnold, J. A., Romanowsky, A. J., Brodie, J. P., et al. 2013, ArXiv e-prints
Barden, S. C., Sawyer, D. G., & Honeycutt, R. K. 1998, Proc. SPIE Vol. 3355, 3355, 892
Barth, A. J., Ho, L. C., & Sargent, W. L. W. 2002, AJ, 124, 2607
Beers, T. C., Flynn, K., & Gebhardt, K. 1990, Astronomical Journal (ISSN 0004-6256), 100, 32
Bender, R., Surma, P., Doebereiner, S., Moellenhoff, C., & Madejsky, R. 1989, A&A, 217, 35
Bernardi, M., Hyde, J. B., Sheth, R. K., Miller, C. J., & Nichol, R. C. 2007, AJ, 133, 1741
Bertola, F., & Capaccioli, M. 1975, ApJ, 200, 439
Bezanson, R., van Dokkum, P. G., Tal, T., et al. 2009, ApJ, 697, 1290
Binney, J. 1978a, Comments on Astrophysics, 8, 27
—. 1978b, MNRAS, 183, 501
—. 2005, MNRAS, 363, 937
Blanc, G. A., Heiderman, A., Gebhardt, K., Evans, N. J. I., & Adams, J. 2009, ApJ, 704, 842
Blanc, G. A., Adams, J. J., Gebhardt, K., et al. 2011, ApJ, 736, 31
Blanc, G. A., Weinzirl, T., Song, M., et al. 2013, AJ, 145, 138
Blanton, M. R., Eisenstein, D., Hogg, D. W., Schlegel, D. J., & Brinkmann, J. 2005, ApJ, 629, 143
Bois, M., Emsellem, E., Bournaud, F., et al. 2011, MNRAS, 416, 1654
Bruzual, G., & Charlot, S. 2003, MNRAS, 344, 1000
Buitrago, F., Trujillo, I., Conselice, C. J., et al. 2008, ApJ Letters, 687, L61
Burbidge, E. M., Burbidge, G. R., & Fish, R. A. 1961, ApJ, 133, 393
Caon, N., Capaccioli, M., & D'Onofrio, M. 1993, MNRAS, 265, 1013
Cappellari, M. 2013, ApJ Letters, 778, L2
Cappellari, M., & Emsellem, E. 2004, PASP, 116, 138
Cappellari, M., Emsellem, E., Bacon, R., et al. 2007, MNRAS, 379, 418
Cappellari, M., Emsellem, E., Krajnovic, D., et al. 2011, MNRAS, 413, 813
Carollo, C. M., & Danziger, I. J. 1994, MNRAS, 270, 523
Carollo, C. M., Danziger, I. J., Rich, R. M., & Chen, X. 1997, ApJ, 491, 545
Cenarro, A. J., & Trujillo, I. 2009, ApJ Letters, 696, L43
Ceverino, D., Dekel, A., & Bournaud, F. 2010, MNRAS, 404, 2151
Cimatti, A., Cassata, P., Pozzetti, L., et al. 2008, A&A, 482, 21
Coccato, L., Arnaboldi, M., Gerhard, O., et al. 2010, A&A, 519, A95
Coccato, L., Gerhard, O., Arnaboldi, M., et al. 2009, MNRAS, 394, 1249
Cole, S., Lacey, C. G., Baugh, C. M., & Frenk, C. S. 2000, MNRAS, 319, 168
Conroy, C., & Gunn, J. E. 2010, ApJ, 712, 833
Conroy, C., Gunn, J. E., & White, M. 2009, ApJ, 699, 486
Daddi, E., Renzini, A., Pirzkal, N., et al. 2005, ApJ, 626, 680
Damjanov, I., McCarthy, P. J., Abraham, R. G., et al. 2009, ApJ, 695, 101
Davies, R. L., Efstathiou, G., Fall, S. M., Illingworth, G., & Schechter, P. L. 1983, ApJ, 266, 41
Davis, T. A., Alatalo, K., Sarzi, M., et al. 2011, MNRAS, 417, 882
De Lucia, G., Springel, V., White, S. D. M., Croton, D., & Kauffmann, G. 2006, MNRAS, 366, 499
de Vaucouleurs, G. 1948, Annales d'Astrophysique, 11, 247
de Zeeuw, T. 1985, MNRAS, 215, 731
de Zeeuw, T., & Franx, M. 1991, ARAA, 29, 239
Dekel, A., Sari, R., & Ceverino, D. 2009, ApJ, 703, 785
Del Burgo, C., Carter, D., & Sikkema, G. 2008, A&A, 477, 105
di Serego Alighieri, S., Vernet, J., Cimatti, A., et al. 2005, A&A, 442, 125
Domínguez Sánchez, H., Pozzi, F., Gruppioni, C., et al. 2011, MNRAS, 417, 900
Dressler, A. 1979, ApJ, 231, 659
Duc, P.-A., Cuillandre, J.-C., Serra, P., et al. 2011, MNRAS, 417, 863
Elmegreen, B. G. 2009, 254, 289
Emsellem, E., Cappellari, M., Peletier, R. F., et al. 2004, MNRAS, 352, 721
Emsellem, E., Cappellari, M., Krajnovic, D., et al. 2007, MNRAS, 379, 401
Emsellem, E., Cappellari, M., Krajnović, D., et al. 2011, MNRAS, 414, 888
Feldmann, R., Carollo, C. M., & Mayer, L. 2011, ApJ, 736, 88
Feldmann, R., Carollo, C. M., Mayer, L., et al. 2010, ApJ, 709, 218
Finkelstein, S. L., Hill, G. J., Gebhardt, K., et al. 2011, AJ, 729, 140
Forbes, D. A., Franx, M., & Illingworth, G. D. 1994, ApJ, 428, L49
Foster, C., Arnold, J. A., Forbes, D. A., et al. 2013, MNRAS, 435, 3587
Franx, M., Illingworth, G., & de Zeeuw, T. 1991, ApJ, 383, 112
Franx, M., van Dokkum, P. G., Schreiber, N. M. F., et al. 2008, ApJ, 688, 770
Gabor, J. M., & Davé, R. 2012, MNRAS, 427, 1816
Gebhardt, K., Richstone, D., Kormendy, J., et al. 2000, AJ, 119, 1157
Gebhardt, K., Richstone, D., Tremaine, S., et al. 2003, ApJ, 583, 92
Gerhard, O. E. 1993, MNRAS, 265, 213
Graham, A. W., Driver, S. P., Petrosian, V., et al. 2005, AJ, 130, 1535
Graves, G. J., Faber, S. M., Schiavon, R. P., & Yan, R. 2007, ApJ, 671, 243
Graves, G. J., & Schiavon, R. P. 2008, ApJ Supp, 177, 446
Greene, J. E., & Ho, L. C. 2006, ApJ, 641, 117
Greene, J. E., Murphy, J. D., Comerford, J. M., Gebhardt, K., & Adams, J. J. 2012, ApJ, 750, 32
Greene, J. E., Murphy, J. D., Graves, G. J., et al. 2013, ApJ, 776, 64
Hill, G. J., MacQueen, P. J., Smith, M. P., et al. 2008, in Society of Photo-Optical Instrumentation Engineers (SPIE) Conference Series, Vol. 7014, Society of Photo-Optical Instrumentation Engineers (SPIE) Conference Series
Hilz, M., Naab, T., & Ostriker, J. P. 2013, ApJ, 429, 2924
Hilz, M., Naab, T., Ostriker, J. P., et al. 2012, ApJ, 425, 3119
Ho, L. C., Greene, J. E., Filippenko, A. V., & Sargent, W. L. W. 2009, ApJ Supp, 183, 1
Hoffman, L., Cox, T. J., Dutta, S., & Hernquist, L. 2009, ApJ, 705, 920
Hoffman, L., Cox, T. J., Dutta, S., & Hernquist, L. 2010, ApJ, 723, 818
Hopkins, P. F., Bundy, K., Murray, N., et al. 2009, MNRAS, 398, 898
Huchra, J. P., Macri, L. M., Masters, K. L., et al. 2012, ApJ Supp, 199, 26
Illingworth, G. 1977, ApJ Letters, 218, L43
Jesseit, R., Naab, T., & Burkert, A. 2005, MNRAS, 360, 1185
Jesseit, R., Naab, T., Peletier, R. F., & Burkert, A. 2007, MNRAS, 376, 997
Jimmy, Tran, K.-V., Brough, S., et al. 2013, ApJ, 778, 171
Jorgensen, I., Hjorth, J., Franx, M., & van Dokkum, P. 1997, AAS, 190, 780
Joung, M. R., Cen, R., & Bryan, G. L. 2009, ApJ Letters, 692, L1
Kelson, D. D., Zabludoff, A. I., Williams, K. A., et al. 2002, ApJ, 576, 720
Kereš, D., Katz, N., Fardal, M., Davé, R., & Weinberg, D. H. 2009, MNRAS, 395, 160
Kereš, D., Katz, N., Weinberg, D. H., & Davé, R. 2005, MNRAS, 363, 2

Khochfar, S., & Silk, J. 2006, ApJ Letters, 648, L21
Khochfar, S., Emsellem, E., Serra, P., et al. 2011, MNRAS, 417, 845
Kormendy, J. 1984, ApJ, 287, 577
Kormendy, J., & Bender, R. 1996, ApJ Letters, 464, L119
Kormendy, J., Fisher, D. B., Cornell, M. E., & Bender, R. 2009, ApJ Supp, 182, 216
Krajnović, D., Cappellari, M., de Zeeuw, P. T., & Copin, Y. 2006, MNRAS, 366, 787
Krajnović, D., Bacon, R., Cappellari, M., et al. 2008, MNRAS, 390, 93
Krajnovic, D., Emsellem, E., Cappellari, M., et al. 2011, MNRAS, 414, 2923
Krick, J. E., Bernstein, R. A., & Pimbblet, K. A. 2006, AJ, 131, 168
Lackner, C. N., Cen, R., Ostriker, J. P., & Joung, M. R. 2012, MNRAS, 425, 641
Lackner, C. N., & Gunn, J. E. 2012, MNRAS, 421, 2277
Longhetti, M., Saracco, P., Severgnini, P., et al. 2007, MNRAS, 374, 614
Loubser, S. I., Sansom, A. E., Sanchez-Blazquez, P., Soechting, I. K., & Bromage, G. E. 2009, VizieR On-line Data Catalog, 739, 11009
Mandelbaum, R., et al. 2005, MNRAS, 361, 1287
McConnell, N. J., Ma, C.-P., Murphy, J. D., et al. 2012, ApJ, 756, 179
McElroy, D. B. 1998, VizieR Online Data Catalog, 210, 105
McNeil-Moylan, E. K., Freeman, K. C., Arnaboldi, M., & Gerhard, O. E. 2012, A&A, 539, 11
Méndez, R. H., Riffeser, A., Kudritzki, R.-P., et al. 2001, ApJ, 563, 135
Murphy, J., Gebhardt, K., Greene, J. E., & Graves, G. 2013, Probes of Dark Matter on Galaxy Scales, 50103
Murphy, J. D., Gebhardt, K., & Adams, J. J. 2011, ApJ, 729, 129
Naab, T., Johansson, P. H., & Ostriker, J. P. 2009, ApJ Letters, 699, L178
Naab, T., Johansson, P. H., Ostriker, J. P., & Efstathiou, G. 2007, ApJ, 658, 710
Naab, T., Oser, L., Emsellem, E., et al. 2013, ArXiv e-prints
Oogi, T., & Habe, A. 2013, Monthly Notices of the Royal Astronomical Society, 428, 641
Oosterloo, T., Balcells, M., & Carter, D. 1994, MNRAS, 266, L10
Oser, L., Naab, T., Ostriker, J. P., & Johansson, P. H. 2012, ApJ, 744, 63
Oser, L., Ostriker, J. P., Naab, T., Johansson, P. H., & Burkert, A. 2010, ApJ, 725, 2312
Paturel, G., Petit, C., Prugniel, P., et al. 2003, A&A, 412, 45
Pota, V., Graham, A. W., Forbes, D. A., et al. 2013, MNRAS, 433, 235
Proctor, R. N., Forbes, D. A., Romanowsky, A. J., et al. 2009, MNRAS, 398, 91
Remus, R.-S., Burkert, A., Dolag, K., et al. 2013, ApJ, 766, 71
Rix, H.-W., & White, S. D. M. 1992, MNRAS, 254, 389
Romanowsky, A. J., & Fall, S. M. 2012, ApJ Supp, 203, 17
Saracco, P., Gargiulo, A., & Longhetti, M. 2012, MNRAS, 422, 3107
Sargent, W. L. W., Schechter, P. L., Boksenberg, A., & Shortridge, K. 1977, ApJ, 212, 326
Schiavon, R. P. 2007, ApJ Supp, 171, 146
Serra, P., Oosterloo, T., Morganti, R., et al. 2012, MNRAS, 422, 1835
Serra, P., Oser, L., Krajnovic, D., et al. 2014, arXiv.org, 3180
Simkin, S. M. 1974, A&A, 31, 129
Statler, T. S. 1991, AJ, 102, 882
Strader, J., Romanowsky, A. J., Brodie, J. P., et al. 2011, ApJ Supp, 197, 33
Strateva, I., Ivezić, Ž., Knapp, G. R., et al. 2001, AJ, 122, 1861
Szomoru, D., Franx, M., & van Dokkum, P. G. 2012, ApJ, 749, 121
Taranu, D. S., Dubinski, J., & Yee, H. K. C. 2013, ApJ, 778, 61
Thomas, J., Saglia, R. P., Bender, R., et al. 2011, MNRAS, 415, 545
Toft, S., van Dokkum, P., Franx, M., et al. 2007, ApJ, 671, 285
Tonry, J., & Davis, M. 1979, AJ, 84, 1511
Tremblay, B., & Merritt, D. 1995, AJ, 110, 1039
—. 1996, AJ, 111, 2243
Trujillo, I., Feulner, G., Goranova, Y., et al. 2006, MNRAS, 373, L36
van de Sande, J., Kriek, M., Franx, M., et al. 2011, ApJ Letters, 736, L9
van de Sande, J., Kriek, M., Franx, M., et al. 2013, ApJ, 771, 85
van den Bosch, R. C. E., van de Ven, G., Verolme, E. K., Cappellari, M., & de Zeeuw, P. T. 2008, MNRAS, 385, 647
van der Marel, R. P., & Franx, M. 1993, ApJ, 407, 525
van der Wel, A., Franx, M., van Dokkum, P. G., et al. 2006, ApJ Letters, 636, L21
van der Wel, A., Holden, B. P., Zirm, A. W., et al. 2008, ApJ, 688, 48
van Dokkum, P. G. 2005, AJ, 130, 2647
van Dokkum, P. G., Franx, M., Kriek, M., et al. 2008, ApJ Letters, 677, L5
van Dokkum, P. G., Whitaker, K. E., Brammer, G., et al. 2010, ApJ, 709, 1018
Weijmans, A.-M., Cappellari, M., Bacon, R., et al. 2009, MNRAS, 398, 561
Whitaker, K. E., Kriek, M., van Dokkum, P. G., et al. 2012, ApJ, 745, 179
Whitmore, B. C., McElroy, D. B., & Tonry, J. L. 1985, ApJ Supp, 59, 1
Wu, X., Gerhard, O., Naab, T., et al. 2014, MNRAS
Yang, X., Mo, H. J., van den Bosch, F. C., et al. 2007, ApJ, 671, 153
Yoachim, P., Roškar, R., & Debattista, V. P. 2010, ApJ Letters, 716, L4
York, D. G., Adelman, J., Anderson, Jr., J. E., et al. 2000, AJ, 120, 1579

APPENDIX

TESTS FOR ROBUSTNESS OF THE KINEMATIC FITS

We show here the results of a series of tests conducted to characterize the robustness of our fits to S/N, continuum fitting, shape of the LOSVD, template mismatch and masking of emission lines. These results were used to motivate our fiducial choice of wavelength region (4000 Å−5420 Å), our minimum S/N threshold, the degree of our continuum polynomial fit and the assumption of a Gaussian LOSVD.

S/N Thresholds

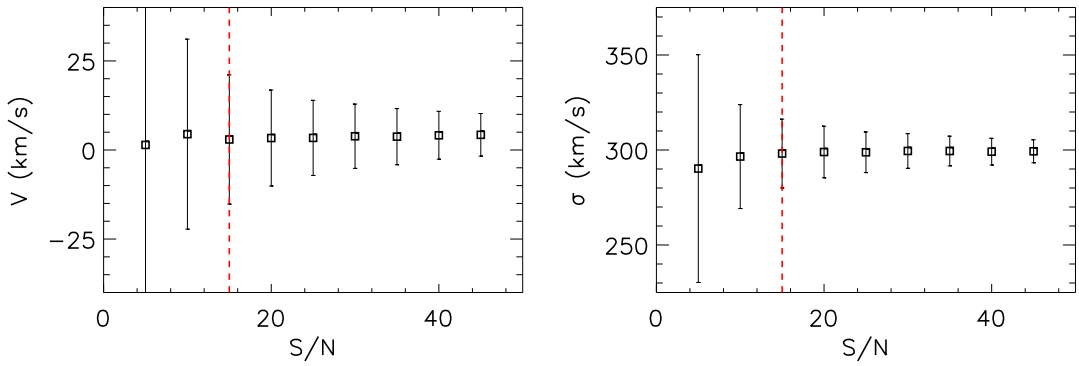

Figure A.1. S/N vs. measured kinematics for a Gaussian LOSVD of mean zero and dispersion 300 km s^{-1}. Error bars show 1-σ uncertainties on the derived values estimated over 100 noise realisations. Values are averaged over the whole library of templates. Our chosen threshold of S/N = 15 is also shown (red dashed line).

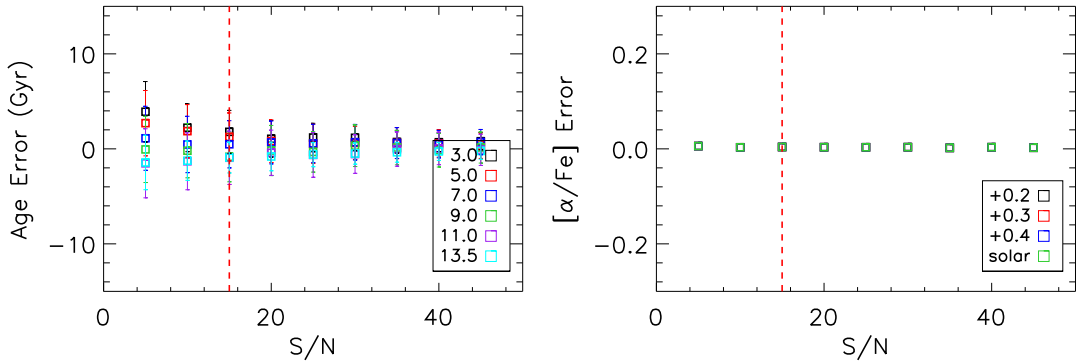

Figure A.2. S/N vs. galaxy characteristics inferred from the best fit templates. We show errors in the inferred age as a function of template age in Gyr (right) and errors in the inferred metallicity as a function of template metallicity in [α/Fe] (left). Error bars again show 1-σ uncertainties, and our chosen S/N threshold is overplotted in red.

We begin by briefly testing the response of pPXF to varying S/N, in order to justify our minimum S/N threshold of 15. This is done by fitting each of the templates in our library, convolved with a Gaussian LOSVD with mean zero and dispersion 300 km s^{-1}, over a variety of S/N. A single realisation, at a given S/N, is found by adding Gaussian random noise to each pixel with a standard deviation set by the pixel flux divided by S/N. When this is repeated over 100 Monte Carlo iterations at each S/N we characterise the bias and scatter in our kinematic fits as a function of S/N. Fits are made using the whole library of templates so that we don't underestimate the scatter, and the process is repeated for each template to test for any systematic effects with galaxy templates. We test over our fiducial range of 4000 Å−5420 Åand since the degree of the continuum polynomial is unimportant for this test, we assume a low order polynomial of degree 4.

The results, shown in Figure A.1, firstly show no bias in the derived dispersions as a function of S/N. There is perhaps a slight bias in the inferred velocity (of $\sim$ 5 km s^{-1}), however this is significantly smaller than both the velocity uncertainty and the pixel separation. The uncertainty in the derived dispersions rise fairly dramatically

for S/N $\lesssim$ 10. We therefore conservatively adopt a minimum S/N threshold of 15, where uncertainties are around $\pm$15 km s^{-1}.

As a sanity check, we also consider how accurately our best fit templates represent the characteristics of the input template. We show in Figure A.2 the errors in our derived ages, and metallicities. The inferred ages, and in particular metallicities, of our fits tend to be quite accurate. At low S/N, older galaxies tend to be biased downwards by $\sim$ 1 Gyr and the reverse holds true for the youngest galaxies. This bias, combined with the spread of $\sim$ 2 Gyr at a S/N of 15, means that any estimates of galactic age based on our fits are likely to be uncertain by at least 3 Gyr.

Degree of the Hermite Polynomial

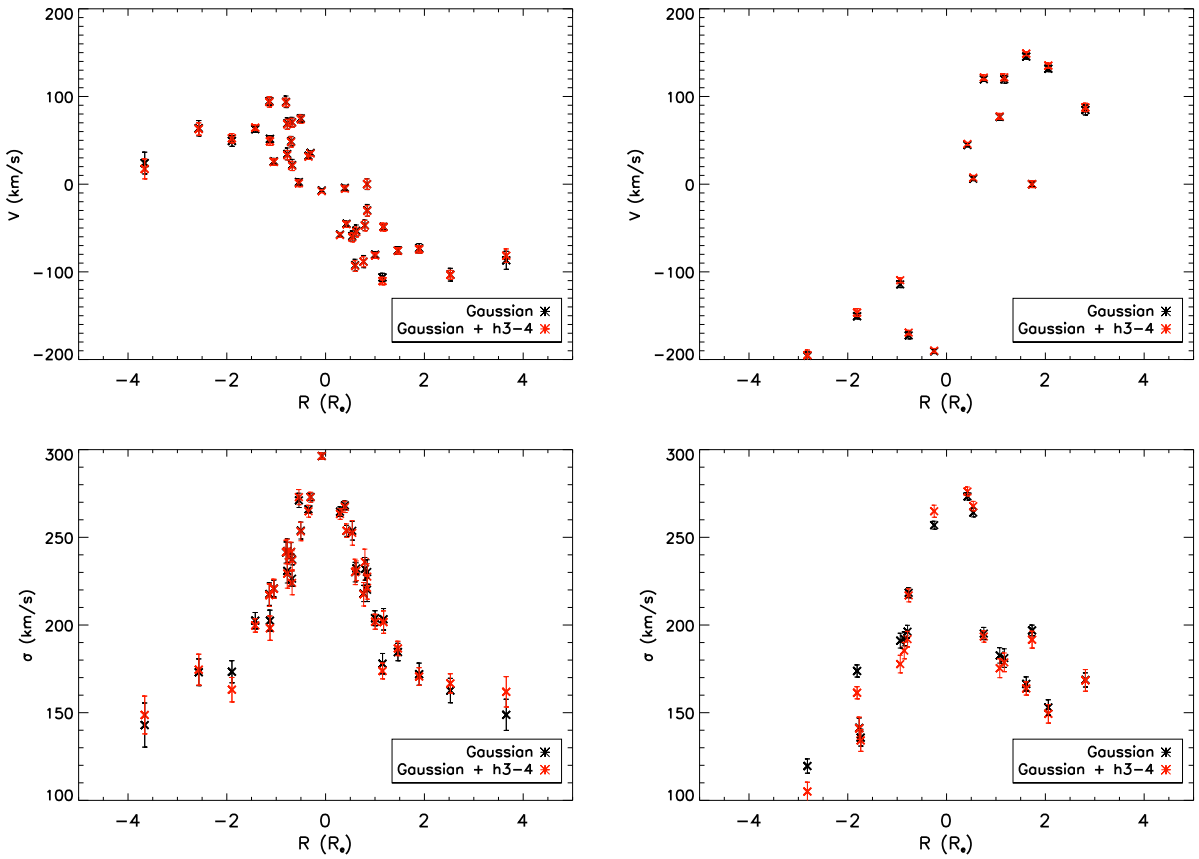

Figure A.3. Velocity (top) and dispersion (bottom) profiles with radius of galaxies NGC 4952 (left) and NGC 426 (right). We compare the profiles calculated using a Gaussian LOSVD (black) and a 4th order Gauss-Hermite series (red).

The effect of including Hermite polynomials of differing degree to the LOSVD function specified in pPXF has also been addressed in some detail by Emsellem et al. (2004). Since pPXF selects against large deviations from Gaussianity, we do not expect the exclusion of higher order hermite moments to create significant systematic errors. We simply ask whether characteristic galaxies in our sample show any systematic differences when we choose to model the LOSVD as a 4th order Gauss-Hermite series.

Figure A.3 shows the velocity and dispersion profiles for galaxies NGC 4952 and NGC 426 calculated both with and without 3rd and 4th order Hermite terms. In both cases we find almost no difference in the velocity profiles as expected. More importantly, the dispersion profiles appear to show no significant differences when we model h_3 and h_4. Arguably, there is a trend towards slightly lower dispersion in the higher order case, particularly at large radius or equivalently lower S/N. This again makes sense since some of the LOSVD power is shifted from the Gaussian term to the Hermite series, lowering the dispersion. However, any deviations are well within 1-σ and below $\sim$ 5 km s^{-1}so we may safely ignore them, and accurately model the LOSVD as a Gaussian alone.

Absorption Features

Although pixel-fitting is robust at relatively low S/N, it can be quite sensitive to template mismatch, which introduces feature-dependent systematics into our dispersion estimates. To investigate how robust we are to this problem, we therefore compare results from a variety of different wavelength regions, centered on different strong spectral features: Ca H+K (3650 Å−4050 Å), G-Band(4215 Å−4575 Å), Hβ (4445 Å−4975 Å), MgIb (4900 Å−5420 Å) and Fe

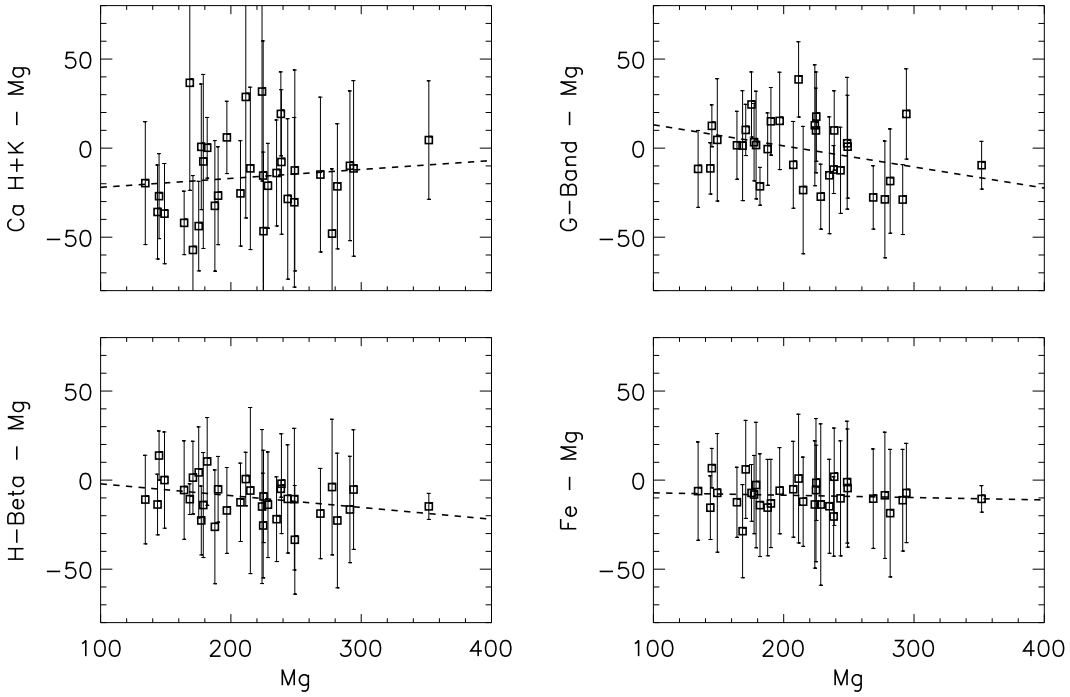

Figure A.4. A comparison between dispersions in the Ca H+K region (3650 Å- 4050 Å), the G-Band (4215 Å−4575 Å), Hβ, (4445 Å−4975 Å), the MgIb region (4900 Å−5420 Å) and the Fe lines redward of MgIb (5250 Å−5820 Å). We show the median offset from the MgIb measurement in all central fibers for each galaxy. Error bars represent standard deviations in the offset distribution and the line of best fit to the offset distribution is shown as a dashed line.

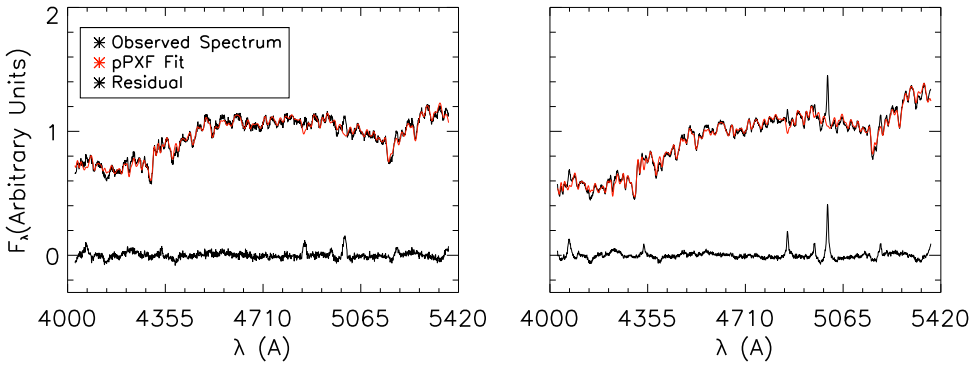

Figure A.5. Fits to the central fibers of galaxies NGC426 (left) and NGC7509 (right), both of which show strong emission lines characteristic of AGN.

(5250 Å−5820 Å), where for the Fe region, we mask out wavelengths between 5570 and 5610 Å, which often shows strong emission lines. Since each of these regions is relatively small, the continuum is fit well enough by a fourth order Legendre polynomial, and uncertainties of less than $\sim 2\%$ are introduced by fitting any polynomial of order between $\approx 2-6$.

We compare regions by taking all of the central fibers from a given galaxy, evaluating the fit in each region and then calculating offsets from the MgIb measurements. Results showing the median and standard deviation of the offset distribution for each galaxy are shown in Figure A.4. We firstly note that, in general, there doesn't appear to be a significant offset between any of the different features in the sense that most galaxies show a median offset consistent with zero. Importantly, the average offset between regions including both MgIb and Fe blends and Fe blends alone appears to be less than ~ 10 km s^{-1}, significantly smaller than the discrepancies found in e.g. Barth et al. (2002). This is perhaps unsurprising, as our set of templates include a range in [α/Fe] above solar, but is nevertheless reassuring.

The Hβ, MgIb and Fe regions align quite well over the range $150 < \sigma < 300$ km s^{-1}, with discrepancies limited to

about ± 30 km s^{-1}and almost negligible mean offsets. By contrast Ca H+K, shows a mean offset of close to 20 km s^{-1} alongside a much larger scatter. This is relatively unsurprising as the continuum drops sharply near 4000Å, and the line shape is quite sensitive to spectral type (see discussion and further references in Greene & Ho 2006).

The only possibly problematic region therefore appears to be the G-Band, which shows a mild trend with dispersion, underestimating the dispersion of the largest galaxies by up to ~ 20 km s^{-1}. The offset is largely due to the presence of a small number of outlying galaxies with large positive offsets from the MgIb region. In particular, NGC 426 and NGC 7509 show G-Band offsets of between +30 and +40 km s^{-1}. Figure A.5 shows the central fibers of these two galaxies, which both display strong emission features characteristic of AGN. Our stellar templates cannot fit these features, but their presence in the MgIb and CaH+K spectra has the effect of artificially driving down the dispersion in these regions and therefore creating a discrepancy with the relatively smooth G-Band. For instance, the central fibers in NGC 7509 and NGC 426 yield MgIb dispersions of 149.8 ± 1.5 and 207.5 ± 5.9 km s^{-1}respectively. However, if we fit the same region with the strongest lines between 4900 Åand 5120 Åmasked out, these values become 186.7 ± 1.2 and 230.5 ± 3.0 km s^{-1}, a shift of ~ 30 km s^{-1}in each case.

Given the presence of strong emission lines in these two galaxies at least, it doesn't necessarily make sense to blindly fit over a relatively small 500 Å window as these results can be significantly skewed by one or two features. We therefore choose to calculate dispersions over a much larger average region 4000 Å− 5420 Å, which is less affected by the presence of a small number of lines. The central fibers of NGC 426 and NGC 7509, for example, yield dispersions of 190.0 ± 1.1 and 231.1 ± 1.4, broadly consistent with the masked MgIb region. Our chosen region includes all of the G-Band, H-β, MgIb and some Fe lines, which should not pose a problem as these regions show no systematic offsets. However, we exclude shorter wavelengths since, as discussed earlier, the S/N drops precipitously near Ca H+K.

Continuum Fitting

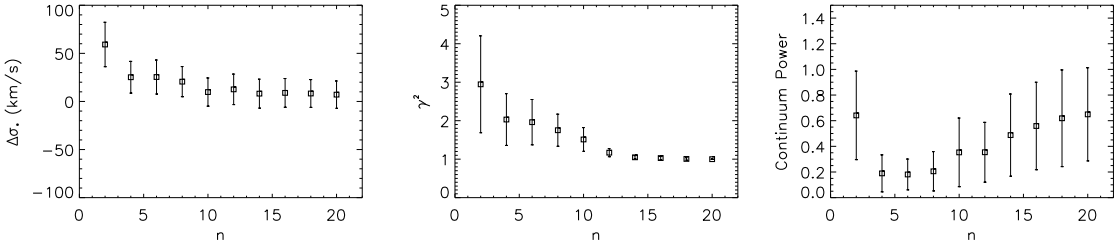

Figure A.6. Measures of goodness of fit as a function of continuum polynomial degree (n) for dispersions calculated over our fiducial region 4000 Å−5420 Å. We show systematic offsets from the median of dispersions evaluated over the G-Band (4215 Å−4575 Å), Hβ, (4445 Å−4975 Å), the MgIb (4900 Å−5420 Å) and the Fe lines redward of MgIb (5250 Å−5820 Å) on the left. In the middle we have the χ^2 of the fit to each galaxy normalised by the minimum χ^2. Finally, on the right we show the continuum power as a fraction of the total galaxy power again normalized to the maximum continuum power. Results shown are calculated as averages over the central fibers in all of our galaxies.

Some care must be taken in fitting this larger region, since the continuum is likely to vary a great deal more over a range of ~ 1500 Å. This may not be captured accurately by stellar templates and a 4th order polynomial alone. On the other hand, if we increase the degree of the continuum polynomial too much, we may begin to fit the absorption lines themselves We therefore need to further test the response of pPXF to the degree of the continuum polynomial between 4000 Å and 5420 Å. In particular, we wish to find the right continuum parameter range that strikes a balance between over-simplifying the continuum and over-fitting it, which would tend to draw power from the LOSVD.

We do this by successively fitting the central fibers of each galaxy using a range of higher order polynomials with degree varying between 2 and 20. The derived dispersions are then compared to the dispersions calculated from the G-Band, Hβ, MgIb and Fe regions alone. Figure A.6 shows the resulting systematic offsets from the median dispersion in these regions, the χ^2 of each fit, and the fraction of spectral power in the continuum.

We see that there are systematic offsets of close to ~ 20 km s^{-1} for continuum fits of degree less than 10. Even above this value the fit over our fiducial region slightly overestimates the dispersion relative to the individual regions, but given that there is a small systematic offset between Fe and MgIb regions, this is probably expected. Above 10 there is also a pronounced drop in the χ^2 of the overall fit, however, by this stage we are clearly over-fitting the continuum since the continuum power rises dramatically. We therefore use a 10^{th} order fit, which is found to best balance the competition between underestimating the continuum and introducing false structure on the dispersion scale.

Template Mismatch

As a final sanity check to see how sensitive we are to the issue of template mismatch, we also compare our calculated dispersions to those extracted from a different set of templates. We use Bruzual & Charlot (2003) single-age stellar population models with $\sigma \sim 70$ km s^{-1}resolution as our comparison set, and fit over our fiducial wavelength region. The results, in Figure A.7 show a very tight correlation between the two sets, so either both sets of templates suffer from similar problems or they are both adequate for our set of galaxies.

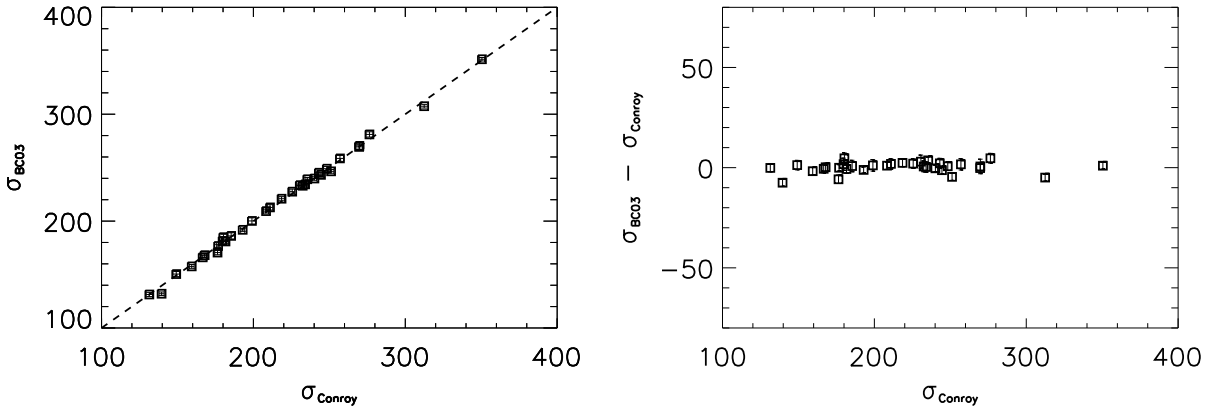

Figure A.7. A comparison between dispersions as calculated from the Conroy et al. (2009) and Bruzual & Charlot (2003) templates. We show both the dispersions and the offsets between the two calculations. We note that the results are remarkably well correlated.

OBSERVED KINEMATICS

We show, in Figures B.1-B.12, full 2D profiles of the velocity and velocity dispersion of all galaxies, as well as 1D kinemetric profiles.

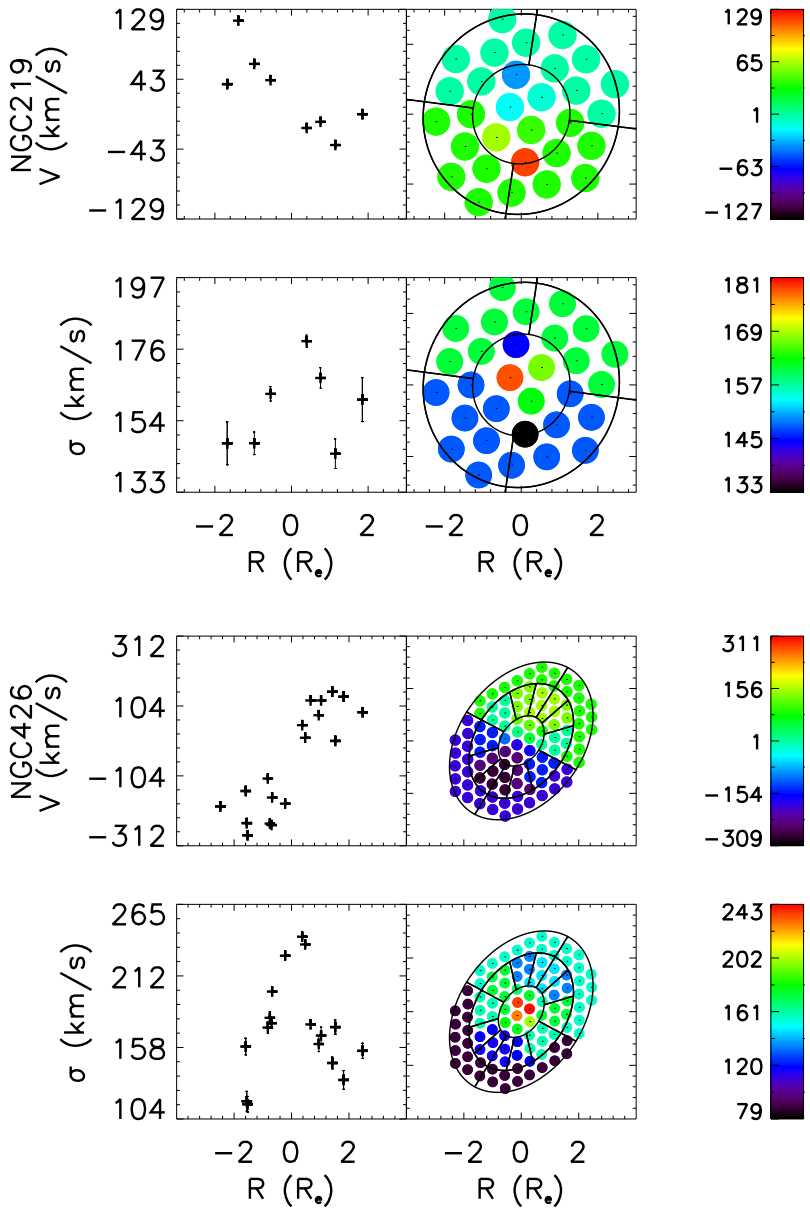

Figure B.1. Maps of the stellar kinematics of all galaxies in our sample. We show from left to right: (i) 1D radial map of stellar mean velocity, where each point corresponds to a different bin at possibly different angular positions (top left) (ii) 2D map of stellar mean velocity (top right), (iii) 1D radial map of stellar velocity dispersion σ (bottom left), (iv) 2D map of σ (bottom right). In a small number of the galaxies, fibres are absent in certain regions due to masking of external sources in those areas. Several galaxies also show non-uniform binning (e.g. IC 1153) due to small astrometric shifts during observation (see e.g. Greene et al. 2013, for more detail). The outermost bin is shown in all cases, but as mentioned in the text, occasionally measurements here needed to be discarded due to excessive masking or limited field-of-view. Finally, low dispersions ($\sigma \lesssim 100$ km s^{-1}, which are generally unreliable with errors $\gtrsim 20\%$, are shown in the 2D maps, but excluded from 1D plots and all calculations of λ and other radial kinematic profiles.

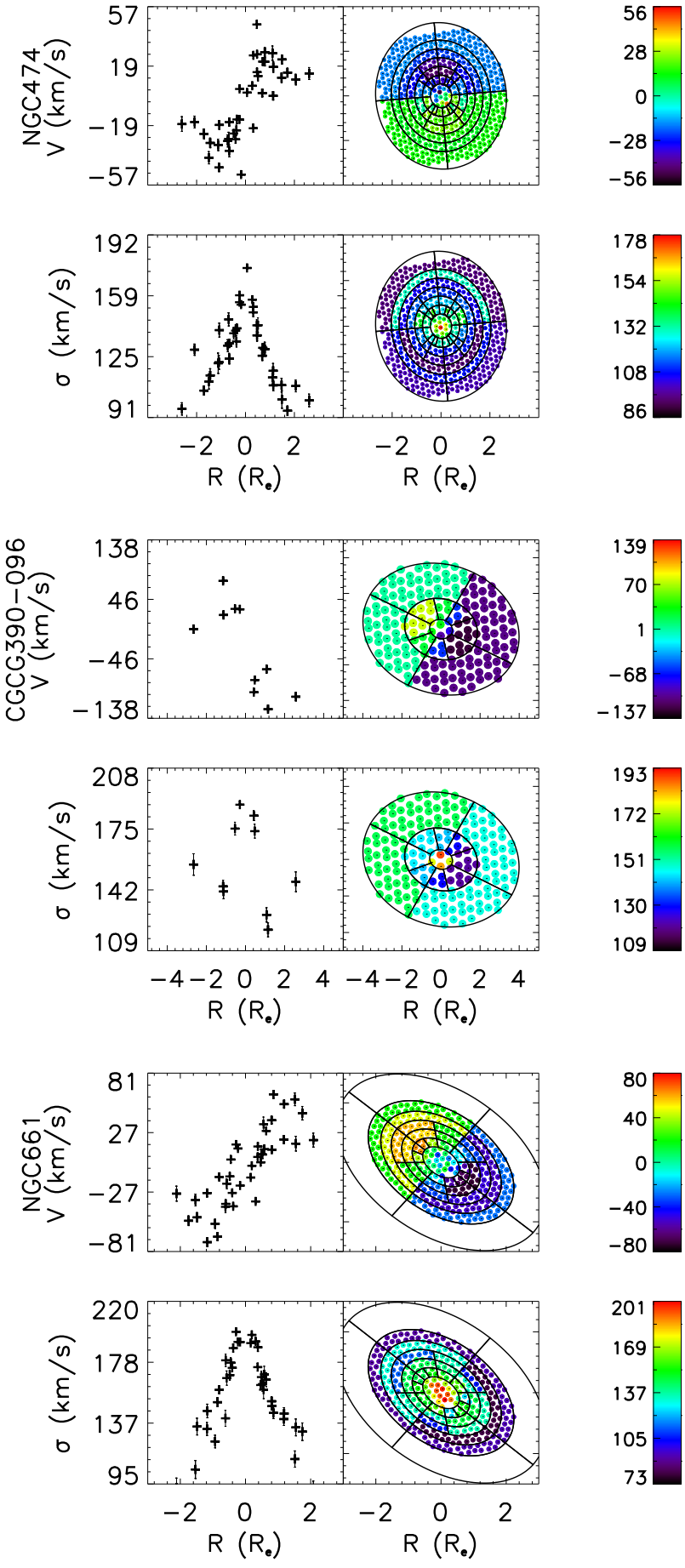

Figure B.2. Continued...

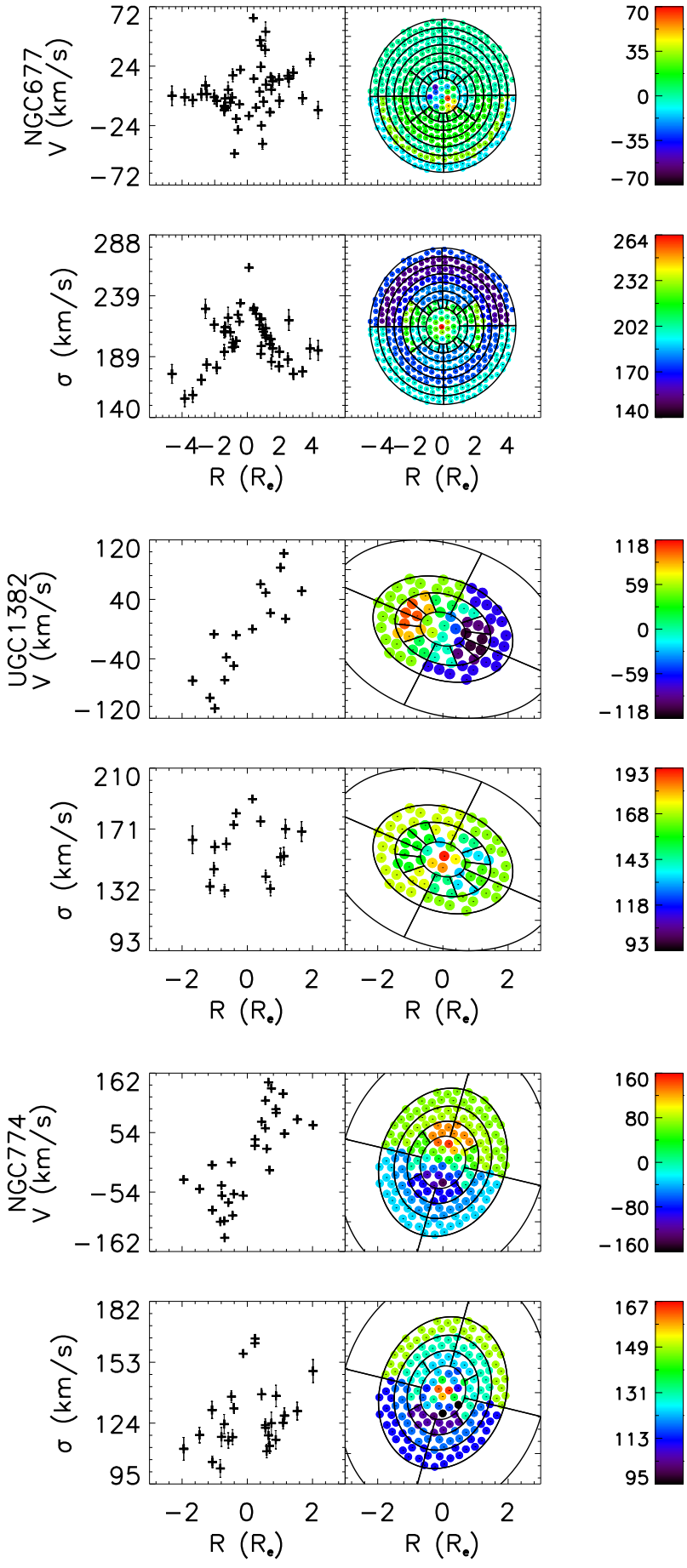

Figure B.3. Continued...

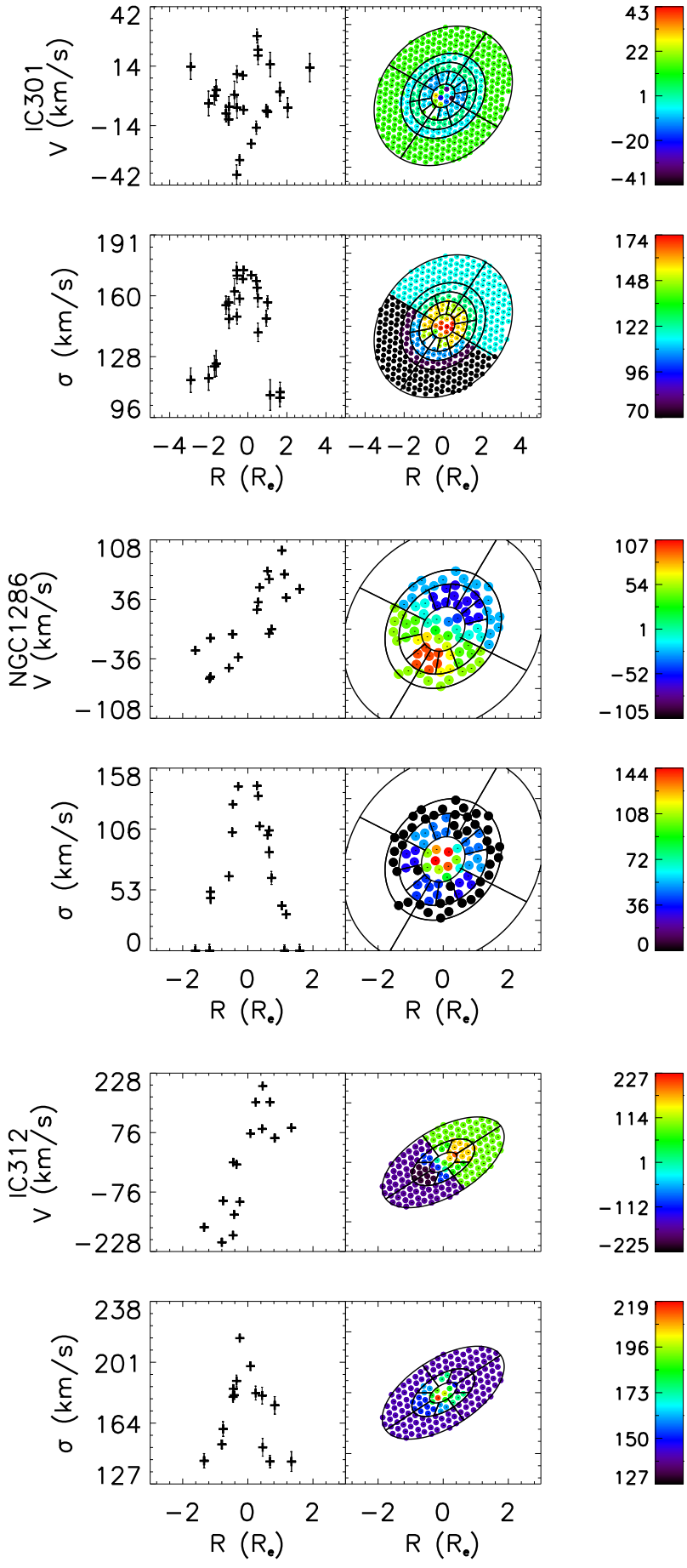

Figure B.4. Continued...

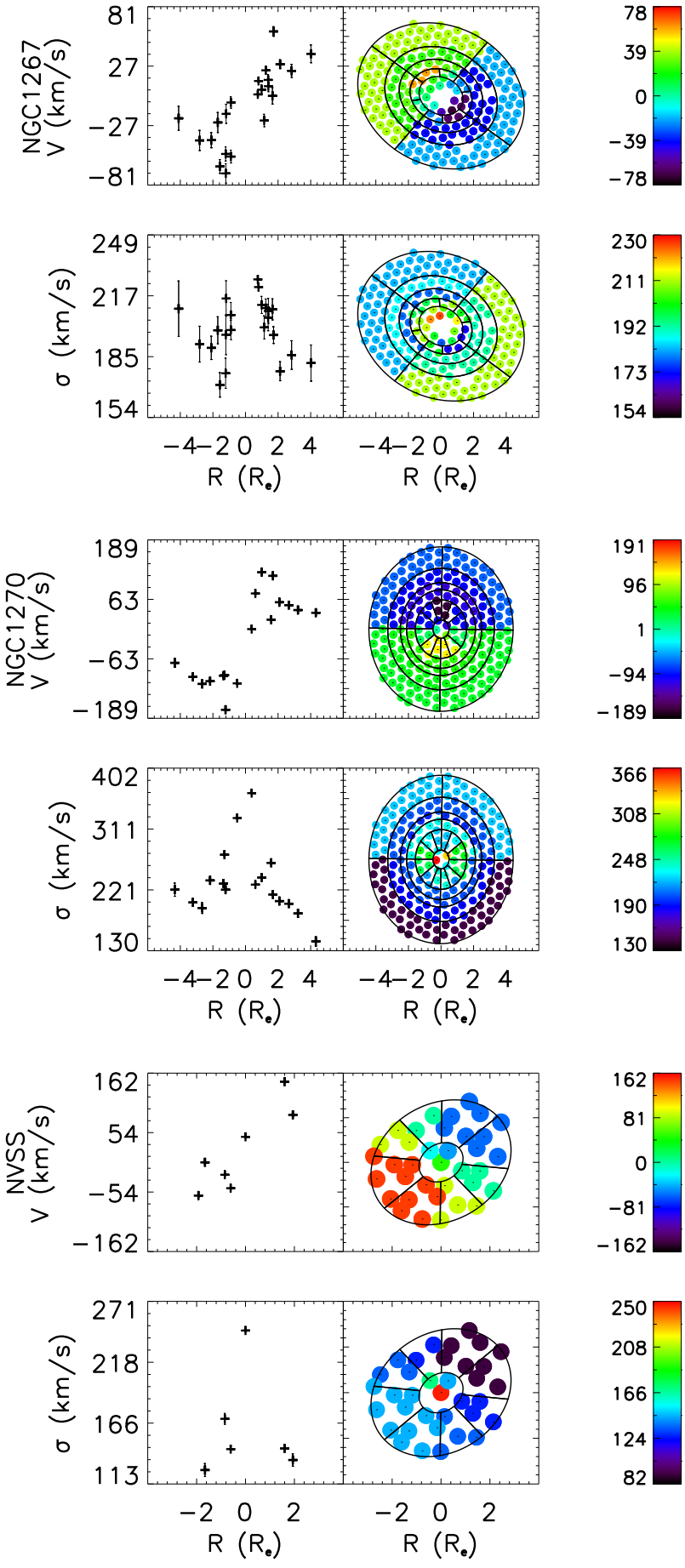

Figure B.5. Continued...

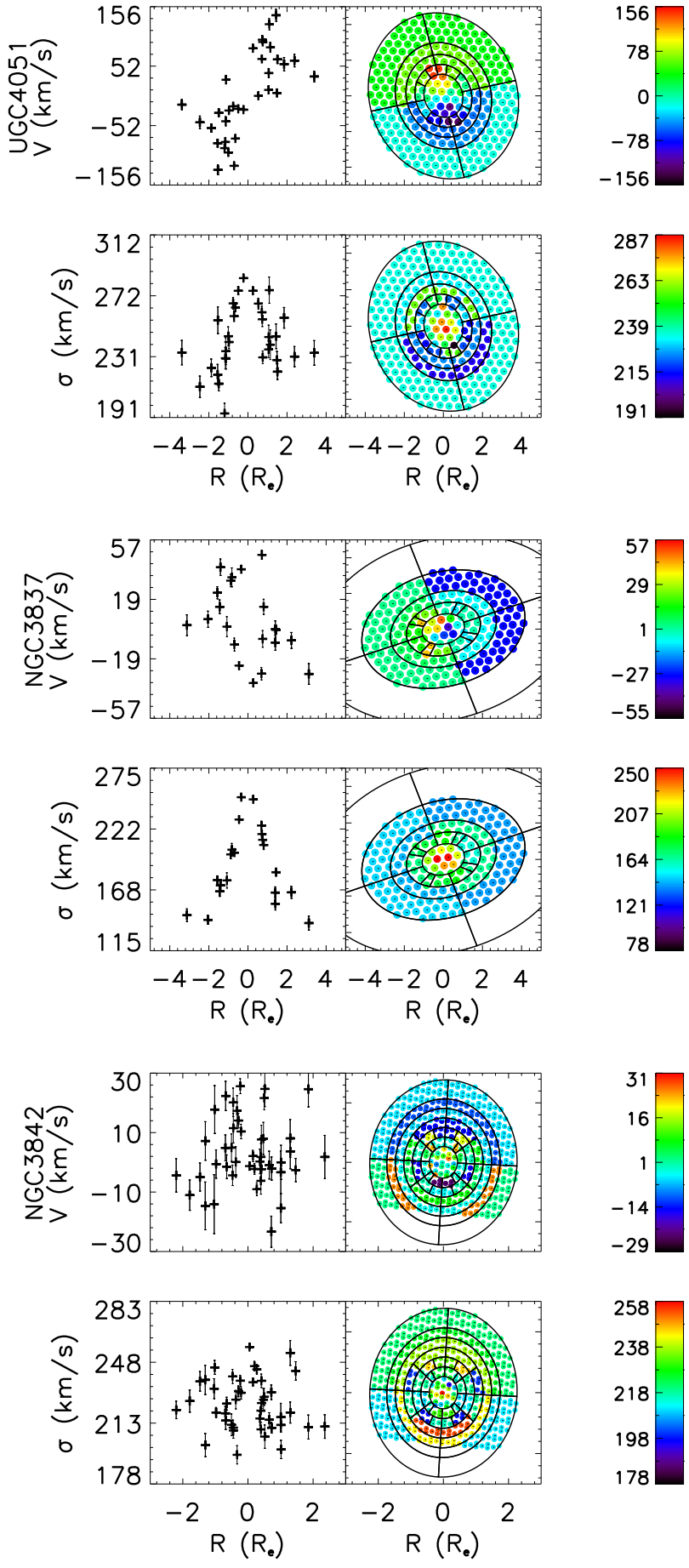

Figure B.6. Continued...

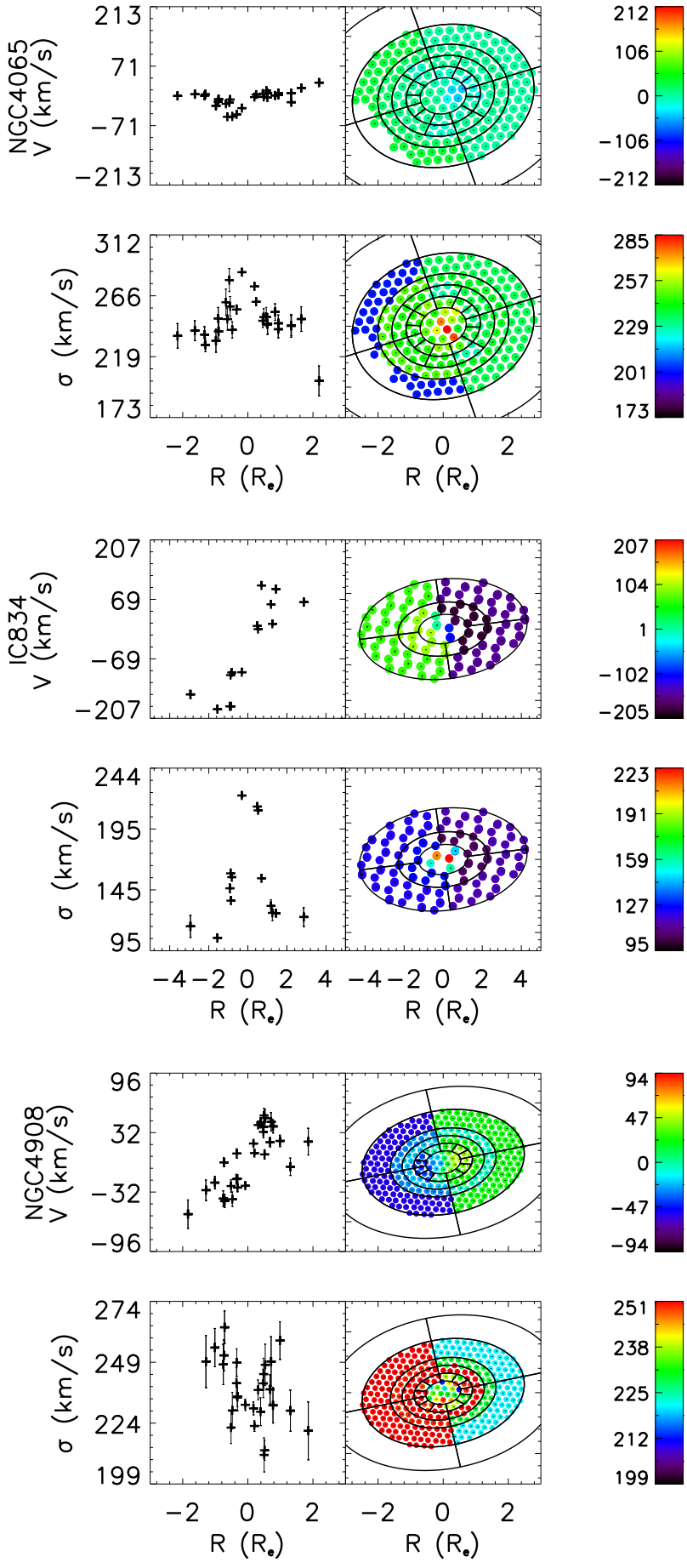

Figure B.7. Continued...

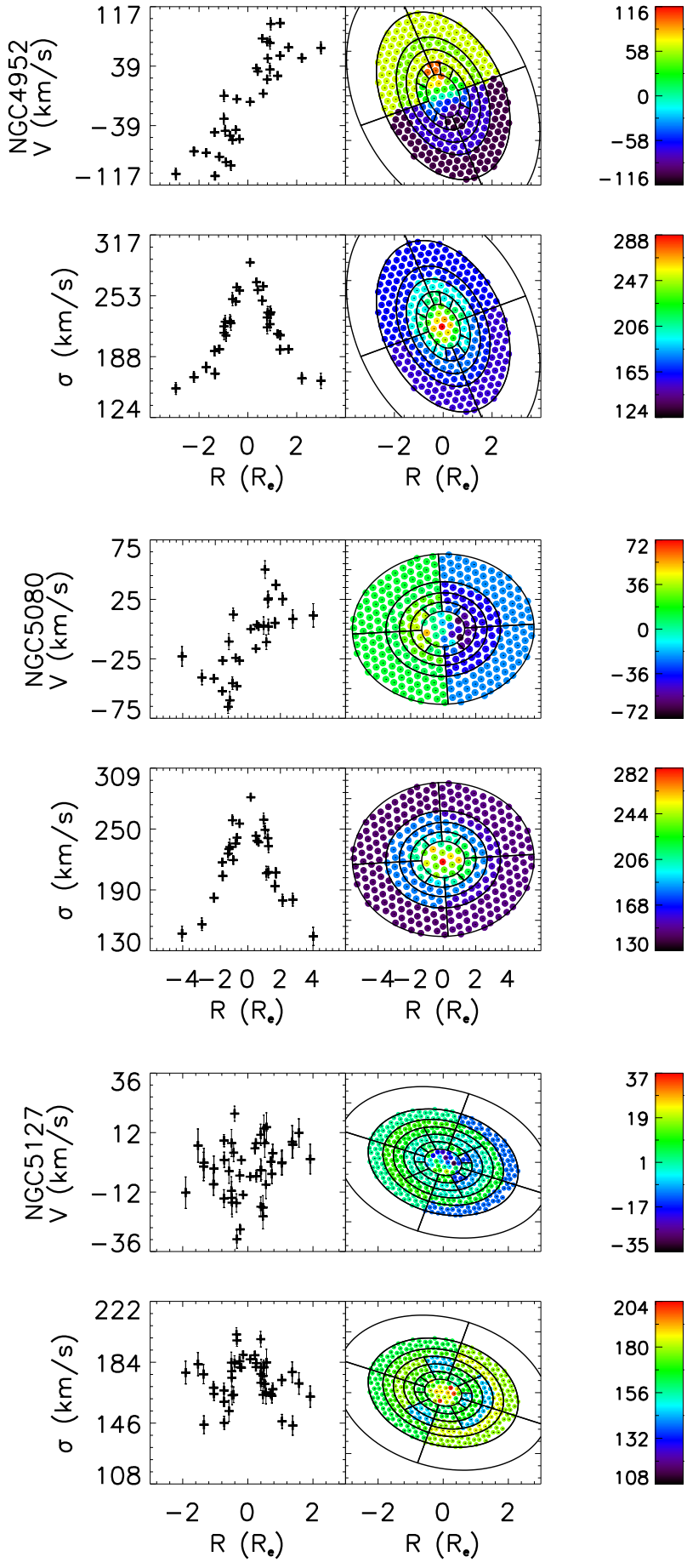

Figure B.8. Continued...

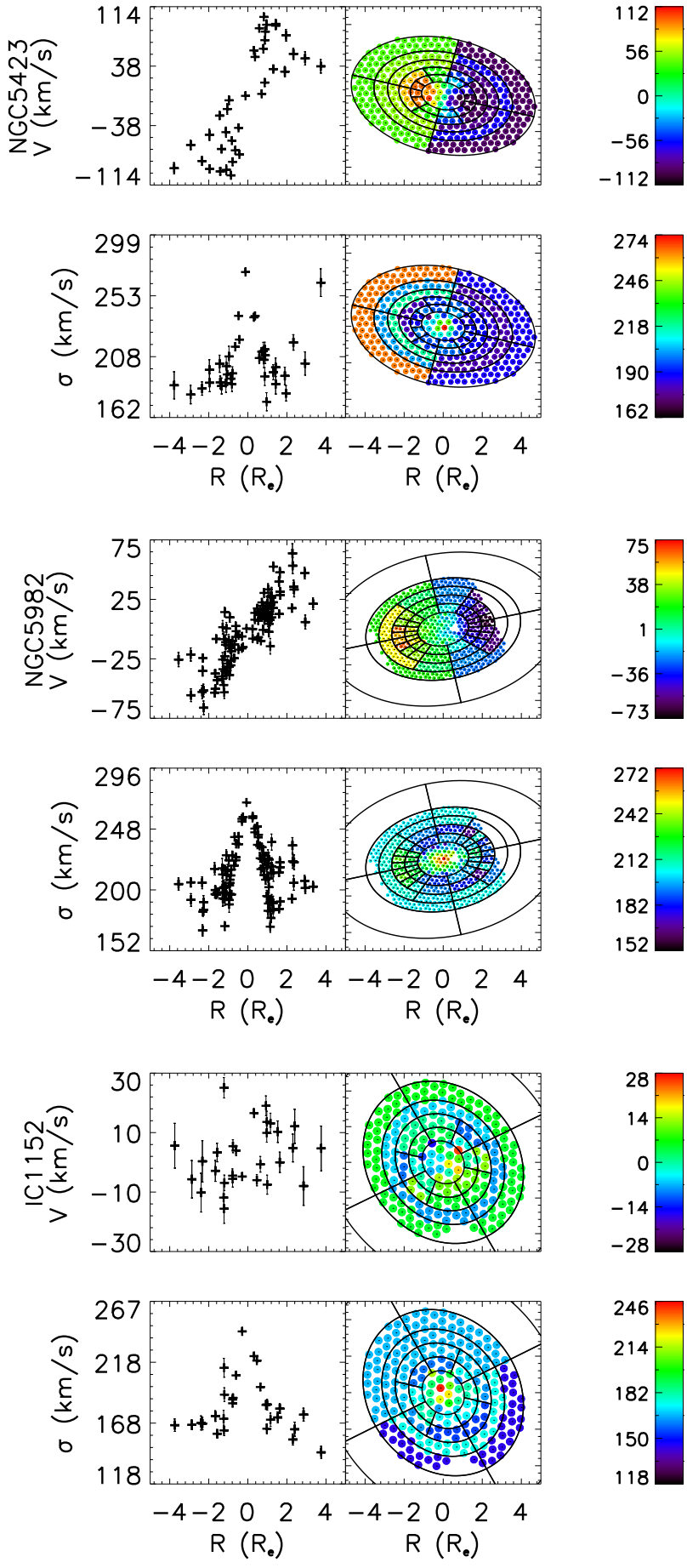

Figure B.9. Continued...

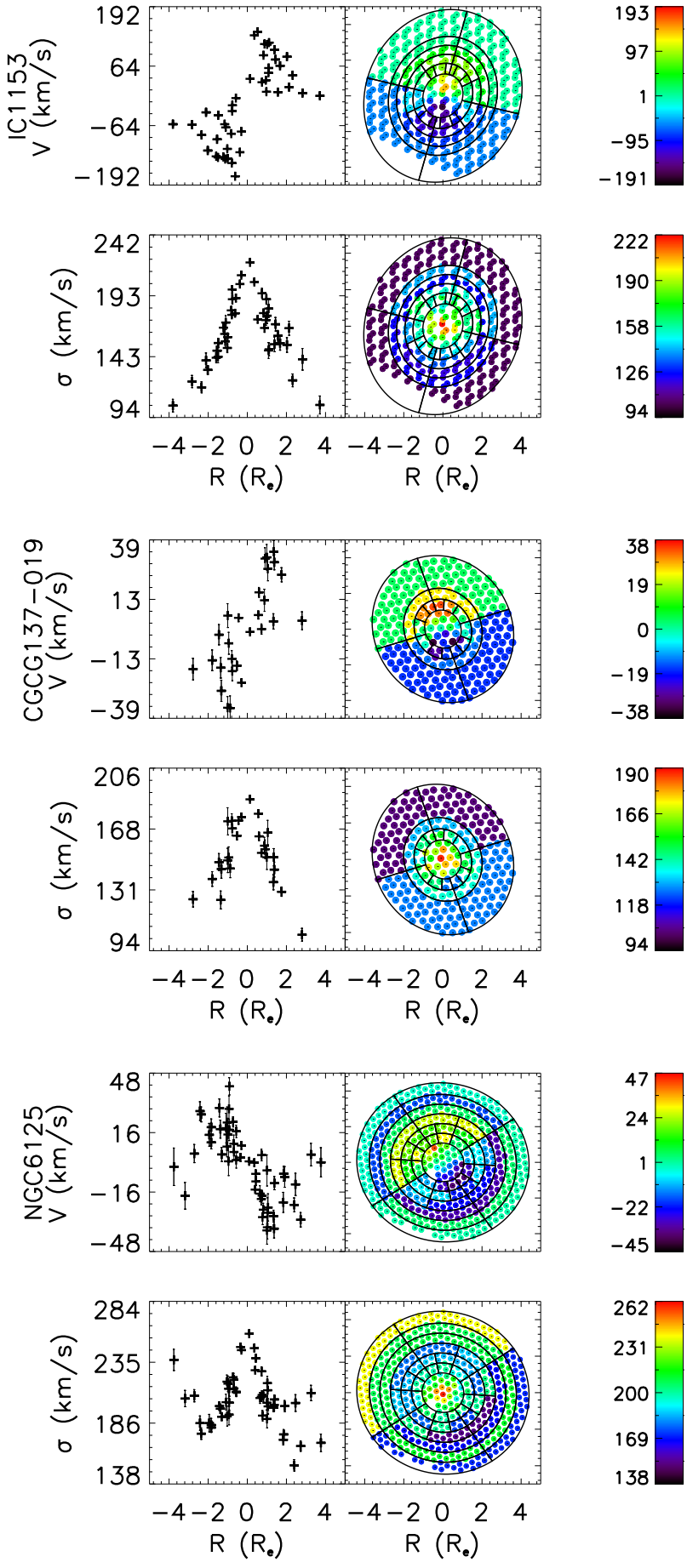

Figure B.10. Continued...

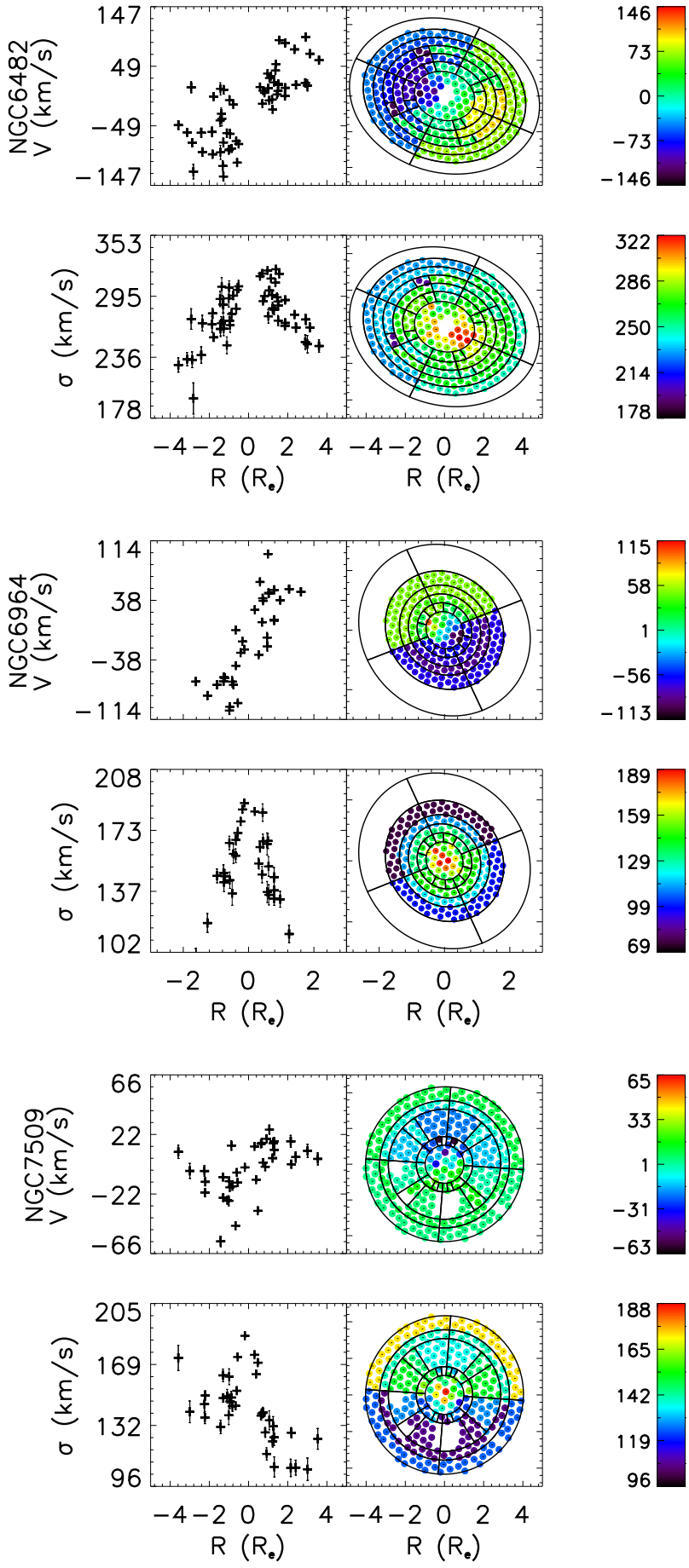

Figure B.11. Continued...

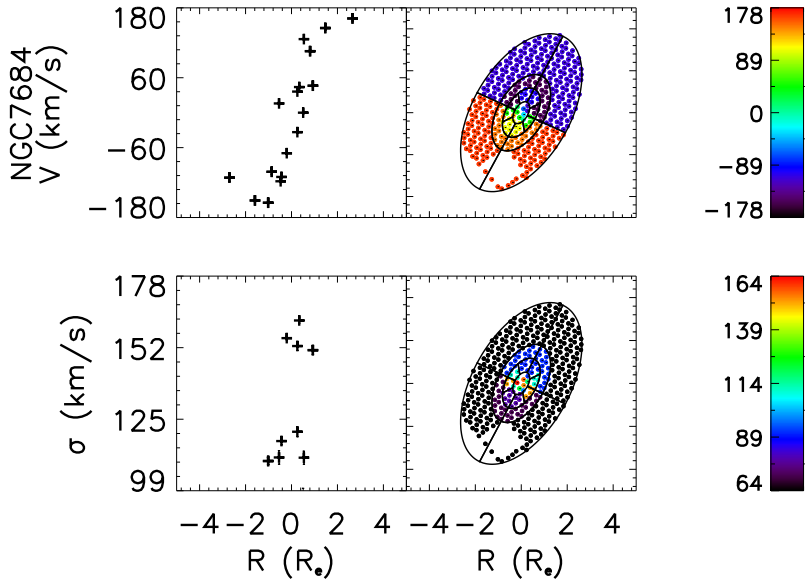

Figure B.12. Continued...